# Water Quality Research Journal

# Effective phosphate removal from sewage water using zerovalent iron nanomaterial as an adsorbent

Ipsita Som[a], Sourav Suman[b], Mouni Roy[a,c], Srimanta Gupta[d] and Rajnarayan Saha [iD][a,*]

[a] Department of Chemistry, National Institute of Technology, Durgapur, West Bengal 713209, India
[b] Department of Earth and Environmental Studies, National Institute of Technology, Durgapur, West Bengal 713209, India
[c] Department of Chemistry, Banasthali University, Banasthali, Rajasthan 304022, India
[d] Department of Environmental Science, Burdwan University, Barddhaman, West Bengal 713104, India
*Corresponding author. E-mail: rnsahanitd@gmail.com

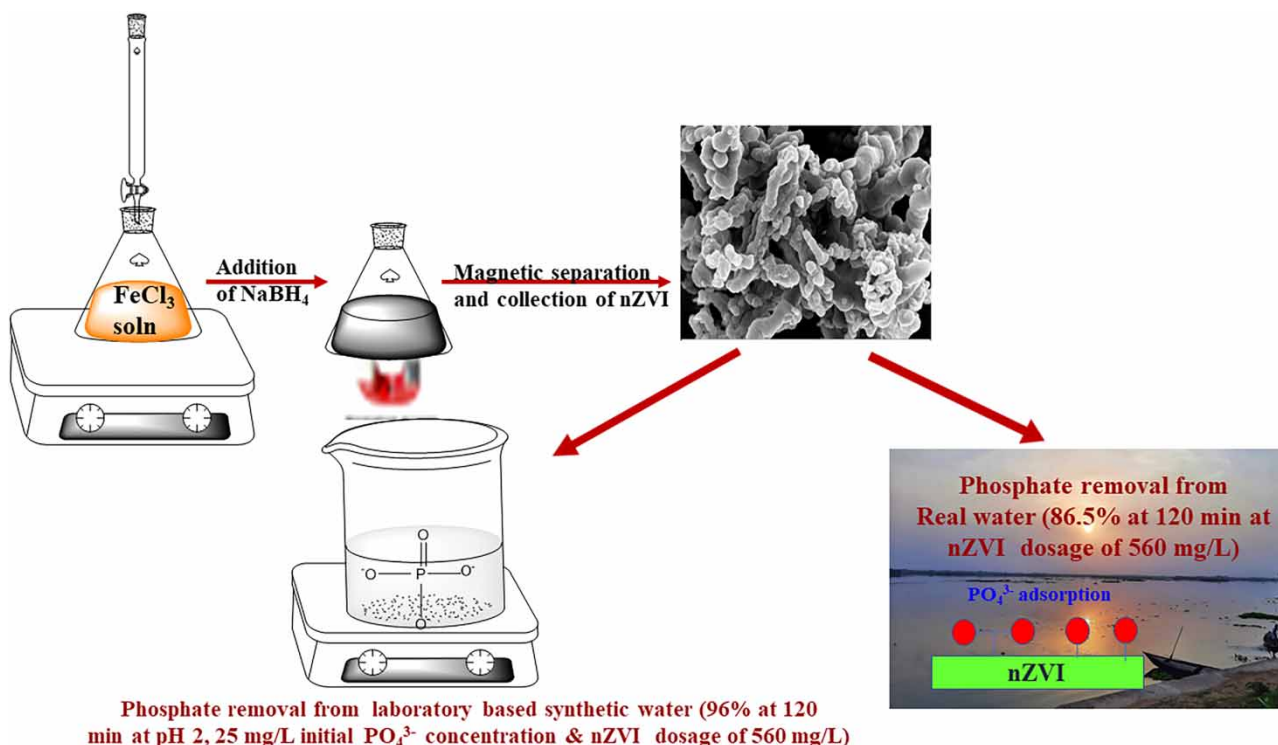[iD] RS, 0000-0001-6167-2271

## ABSTRACT

In recent times, nano zerovalent iron (nZVI) particles have attracted significant attention from researchers for their effectiveness in removing phosphates, a hazardous contaminant found in groundwater and surface water. nZVI possesses some excellent characteristics such as high reactivity, high surface area, and effective surface-to-volume ratio. In this study, nZVI was characterized by X-ray diffraction, Brunauer–Emmett–Teller (BET) surface area analyzer, Fourier transform infra-red (FT-IR), field emission scanning electron microscopy (FESEM), and transmission electron microscopy (TEM) techniques. The effect of variations in nZVI dosage, pH, ionic strength, and coexisting anions on the removal of phosphate from laboratory-based synthetic water was explored. A maximum phosphate removal efficiency of 96% was achieved at an initial phosphate concentration of 25 mg/L, an nZVI dosage of 560 mg/L, and a shaking rate of 500 rpm, and pH 2 was attained within 120 min. Kinetic and equilibrium studies revealed that the adsorption of phosphate follows a pseudo-2nd-order kinetic model and a Temkin isotherm model, respectively. A thermodynamic study confirmed that phosphate adsorption is a spontaneous and endothermic process. Finally, nZVI was proved to be stable up to five cycles. nZVI was further applied for the removal of phosphate from sewage water, which was collected from Saheb bandh, Purulia district of West Bengal, Eastern India.

**Key words**: adsorption, nanoscale zerovalent iron (nZVI), phosphate removal, pollutant, real water sample, wastewater

## HIGHLIGHTS

- Removal of phosphate, a hazardous pollutant, is performed by using zerovalent iron nanomaterial.
- Various reaction parameters, e.g. adsorbent dosage, pH, etc. are optimized.
- Kinetic, thermodynamic, and adsorption isotherm studies were carried out.
- Zerovalent iron nanomaterial is a potential adsorbent for the removal of phosphate from sewage water.

## GRAPHICAL ABSTRACT



Phosphate removal from laboratory based synthetic water (96% at 120 min at pH 2, 25 mg/L initial $PO_4^{3-}$ concentration & nZVI dosage of 560 mg/L)

## 1. INTRODUCTION

Safe drinking water is the most pivotal commodity for the nourishment of life. Potable water, which is used widely for numerous purposes, is getting increasingly polluted today on account of rapid industrialization, man-made activities, and geogenic disturbances. Thus, it is our primary responsibility and a challenge to keep water sources pollutant-free and also keep mineral ion concentration within the permissible levels of toxicity so that water sources can be consumable for human activities (Fu et al. 2014; Brandl et al. 2015; Morillo et al. 2015). Phosphorus (primarily in the form of phosphates) serves as an important nutrient for every existing organism, which, in turn, acts as a major resource for the synthesis of energy carriers, proteins, and nucleic acids in any living cell (Rotzetter et al. 2013).

Nowadays, phosphate ($PO_4^{3-}$) in different forms is one of the vital components that is used in agriculture and industries (fertilizer, domestic detergent, animal feed, food and beverage industries, etc.) (Cordell et al. 2009). The application of phosphorous-containing fertilizers is an integral part of conventional farming practices that produce food for billions of people (UNEP 2011). Besides, the available quantity of this nutrient controls the growth of algae and aquatic plants and helps sustain aquatic ecosystems. But an exponential growth of population and rapid industrialization leads and is leading to an increase in the amount of phosphate used in both soil and water. Thus, this industrial and agricultural runoff leads to excessive liberation and the accumulation of phosphate in water bodies. This may induce several detrimental environmental effects, including eutrophication (anomalous flourishment of seaweeds and marine plants) (Chouyyok et al. 2010). It is observed that the eutrophication process causes a gradual depletion of dissolved oxygen content, which results in the death of several aquatic species (Zhao et al. 2009). The algae growing in long strands often twine around boat propellers and hamper transportation (Ansari et al. 2011). Eutrophic waters tend to be scummy, cloudy, or even soupy green. The rapidly growing aquatic plants may wash onto the shores in storms or high winds, where these plants die, decay, and produce a foul smell all around such water bodies. Enhanced eutrophication also indirectly hampers the economic development of communities that depend on aquatic food and other resources (Cleary et al. 2009). The United States Environmental Protection Agency has endorsed the permissible limit of phosphorus in water to be less than 0.1 mg/L to prevent eutrophication (USEPA 1986). Additionally, the Florida Everglades Forever Act endorsed an original acclamation regarding phosphorus concentration in water, which is to be limited within 10 ppb (Florida State Legislature 1994; Arshadi et al. 2015a, 2015b).

In this sense, phosphate recovery and recycling that can be done from waste materials becomes a fundamental element for sustainable management (Jupp *et al.* 2021). However, researchers have gradually focused on the importance of phosphate recovery from wastewater (Kumar & Pal 2015). Agriculture can recycle the P-rich effluents produced in the food chain, directing them to production systems and concomitantly reducing supply risks and ensuring an economically P-stable value (Roy 2017; Jansson *et al.* 2019). Besides, livestock waste and manure contain high concentrations of phosphate (Nancharaiah *et al.* 2016; Tao *et al.* 2016), while the availability of such resources is inadequate. However, by comparison, municipal wastewater possesses the greatest potential for phosphate recovery (Mehta *et al.* 2015). Specifically, it has been reported that municipal wastewater flows contain a rich amount of phosphorus, with about 60,000–70,000 t P/a in Germany (Adam 2011). However, in practice, in developed and developing countries, the process of P recovery is still a challenge and requires greater attention.

In this context, different treatment techniques have been employed to date for the removal of phosphate, which include physio-chemical processes (Mishra *et al.* 2010), chemical precipitation (de-Bashan & Bashan 2004), and biological phosphate removal (Gouider *et al.* 2011). Although these techniques have been and are effective, they have disadvantages. For example, the biological treatment process has a major drawback, in that the transfer of phosphate from liquid to the sludge phase is essential, leading to a decrease in removal efficiency (RE) up to 30% (Stensel 1991). Physico-chemical treatment processes are associated with certain problems (such as high chemical expenses and operational costs as well as complex sludge generation), which make these processes less desirable (Ghoreishi & Haghighi 2003; Sirianuntapiboon *et al.* 2006). The chemical precipitation method has limited applicability in the case of real water samples due to the high disposal cost of the formed precipitate and the use of expensive chemicals (Wang *et al.* 2005).

Against this background, it has been found that among the aforementioned methods, adsorption of phosphate from wastewater by using a suitable non-toxic environment-friendly highly porous adsorbent is the most desirable to control pollution. It is considered to be suitable in terms of less sludge generation, easy operation, and high removal efficacy (Ryu *et al.* 2011; Novillo *et al.* 2014; Tran *et al.* 2015). So far, typical adsorbents, e.g., zeolite, activated carbon, and diatomite, were chosen for the process. However, they come with certain drawbacks such as high production cost, recovery, and separation difficulties from aqueous solutions, hindering the reusability property of adsorbents (Quesada *et al.* 2020). For ameliorated and effective adsorption of phosphate, the use of nanoparticles as adsorbents has emerged as a highly effective strategy because of their higher specific surface area, higher effective surface-to-volume ratio, and chemical as well as biological stability (Wen *et al.* 2014; Ghosh *et al.* 2017).

Recently, nZVI has been broadly utilized for the adsorption of inorganic anions (Wen *et al.* 2014), metalloids (Kanel *et al.* 2005), and metals because of its alluring properties like the higher surface area-to-volume ratio, resulting in the formation of more active sites. In our work, pure nZVI was selected for remediation of phosphate due to its above-mentioned properties, along with the added advantage of improved magnetic behavior, which helps in a facile separation of adsorbents from water samples after treatment processes. Several research groups have utilized suitable nanoscale adsorbents for phosphate removal and the treatment of sewage water. Some literature reports of such groups have been documented.

Arshadi *et al.* observed phosphate adsorption by nitric acid–treated ostrich bone waste–supported nZVI (OBW-HNO$_3$-nZVI) from both synthetic and real (Persian Gulf) water samples. The chain-like structure of OBW-HNO$_3$-nZVI (0.05 g/L dosage) having a Brunauer–Emmett–Teller (BET) surface area of 41.4 m$^2$ g$^{-1}$ shows maximum phosphate RE (100%) at pH 5.0. The removal percentage of phosphate from the waters of the Persian Gulf was calculated to be 99.9% after 30 min (using 0.05 g/L dosage of OBW-HNO$_3$-nZVI) (Arshadi *et al.* 2015a, 2015b). Arshadi *et al.* investigated phosphate uptake by ferrocene-functionalized aluminum–silicate nanoparticles (Si/Al@Fe) from synthetic and real water samples (Persian Gulf). A total of 96.6% adsorption efficiency was found at pH 8 with an initial phosphate concentration of 850 mg/L (0.05 g/L Si/Al@Fe dosage). The phosphate removal percentage from the Persian Gulf waters was found to be 99.9% by utilizing the synthesized adsorbent after 120 min. The results confirm that Si/Al@Fe is a potential adsorbent to uptake phosphate ions from real water at low concentrations (Arshadi *et al.* 2015a, 2015b). Ge *et al.* synthesized 3D flower-like hierarchical iron containing MnO$_2$ hollow microspheres for efficient phosphate removal from synthetic water and eutrophic lake water (Nanfei river located in the Hefei city of China). A total of 98% phosphate removal was obtained when the initial phosphate concentration was 10 mg/L, with the initial solution at pH 7.0 and a fixed adsorbent dosage of 0.5 g/L. However, almost complete phosphate removal from lake water (total phosphate concentration 1.48 mg/L) was achieved with 0.25 g/L of adsorbent dosage (Ge *et al.* 2016). Riahi *et al.* reported fluoride adsorption by synthesized Fe$_3$O$_4$ nanoparticles modified with zirconia (Fe$_3$O$_4$@ZrO$_2$). The fluoride adsorption capacity was found to be 123.9 mg g$^{-1}$ at pH 2.5 (adsorbent dosage 1 mg mL$^{-1}$). The

fluoride adsorption was also carried out on tap water, leading to an appreciable removal of fluoride below its permissible limit (Riahi *et al.* 2015). Sun *et al.* performed a simultaneous removal of nitrate and phosphate by a synthesized solid carbon source/zerovalent iron (SCS/ZVI) composite. Herein, nitrate and phosphate removal rates of $1.1 \pm 0.1$ mg L$^{-1}$ h$^{-1}$ and $0.21 \pm 0.07$ mg L$^{-1}$ h$^{-1}$ were achieved, respectively, at pH 7 (Sun *et al.* 2021).

Considering the above-mentioned studies/discussion, it is evident that excessive phosphate in water bodies and agricultural runoff are very harmful and need the urgent attention of the research community. It is in this context that we decided to focus our attention on the analysis and treatment of real water samples from a neighboring lake (Saheb bandh lake), situated in the north-western part of Purulia district (23.33 °N, 86.37 °E), West Bengal. The soluble reactive phosphorus or orthophosphate ($PO_4^{3-}$) present in lake water generally ranges between 0.223 and 0.95 mg/L season wise, which is much higher than the permissible level of phosphate in drinking water (Siddiqi & Chandrasekhar 2010). Hence, according to the Trophic State Index, eutrophy is observed in this lake water (Dutta *et al.* 2019). Besides, lake water constitutes natural organic matter (NOM) of great quantity, and NOM consists of a complex heterogeneous continuum of high- to low-molecular-weight species exhibiting different water solubilities and reactivities. Generally, different organic acids such as citric acid, humic acid, oxalic acid, and chlorophyll-a persist in lake water as NOMs in very small amounts. Therefore, the competition between the anion forms of acids and phosphate for the active sites of the studied adsorbent becomes irrelevant and negligible. Furthermore, in the presence of appreciable quantities of NOM, nZVI is the most suitable and potential adsorbent for the removal of phosphate from the studied lake water. NOM enhances the mobility of nZVI (Johnson *et al.* 2009). Thus, the aggregation of nZVI reduces markedly, which, in turn, improves the efficiency of phosphate removal by the studied adsorbent (Aiken *et al.* 2011). The presence of NOM not only enhances the mobility of nZVI but also reduces the aggregation of nZVI. This leads to an increase in the stability of nZVI in the aqueous medium, which makes it a better adsorbent (Domingos *et al.* 2009).

In the present study, we have synthesized porous spherical-shaped zerovalent iron nanoparticles via a simple cost-effective reduction method for phosphate removal by varying different reaction parameters. Herein, it is shown that nZVI can be reused for phosphate adsorption up to the fifth cycle. Furthermore, the probable phosphate adsorption mechanism by synthesized nZVI has been elucidated. Finally, the phosphate uptake capacity of the developed adsorbent for practical application in lake water samples has been studied.

## 2. EXPERIMENTAL SECTION

### 2.1. Chemicals

Iron (III) chloride hexahydrate ($FeCl_3 \cdot 6H_2O$, 98%), the precursor of iron, and sodium borohydride ($NaBH_4$, 98%), reducing agent, were purchased from Merck (India). Absolute ethanol (>99.9%), glycerol (>99.5% Emparta, AR grade), sodium hydroxide, and hydrochloric acid used for pH adjustment were purchased from Merck (India). Milli-ultrapure water (18.2 MΩ cm) was collected for making all solutions and for performing all other tests. Stock solutions having a concentration of 1,000 mg/L were prepared from oven-dried potassium phosphate ($K_3PO_4$) purchased from Merck, India, and used to calibrate $PO_4^{3-}$ estimates. Ammonium molybdate [$(NH_4)_6Mo_7O_{24} \cdot 4H_2O$], sulphuric acid ($H_2SO_4$), and stannous chloride ($SnCl_2 \cdot 2H_2O$) were used as reagents.

### 2.2. Synthesis of nanoparticles

nZVI was synthesized as reported earlier (Ghosh *et al.* 2019) according to Scheme S1.

### 2.2.1. Characterization

Different techniques were employed to characterize the synthesized nZVI particles after their preparation. An X-ray diffraction (XRD) study was performed using the PANalytical Xpert PRO XRD unit to investigate the crystalline structure of the obtained particles. During the process, the operating voltage was set at 40 kV. Also, a Cu-K$\alpha$ radiation source having a wavelength of 1.54 Å was used to scan in the range of 10°–75°. A field emission scanning electron microscope (FESEM) study was performed using a Zeiss Sigma field emission scanning electron microscope (SE2 model, 17 kV) in order to examine the surface morphology of nZVI. High-resolution transmission electron microscope (HRTEM) imaging was performed with Tecnai TF20G2ST HRTEM operating at 220 kV voltages. BET surface area experiments were performed at a temperature of −196 °C using a volumetric apparatus. (Micrometrics ASAP 2020 is an automated gas sorption analyzer.) The degassing of all samples was performed under vacuum at 120 °C for 16 h before the adsorption experiments. The BET surface areas of the adsorbents and the pore size were calculated using the BET method and the Barrett–Joyner–Halenda (BJH) method, respectively. Fourier

transform infra-red (FT-IR) spectrum was recorded in the range of 4,000–400 cm$^{-1}$ as KBr pellets using the Nicolet 5700 spectrometer to track changes on the nZVI surface before and after the adsorption experiment.

## 2.3. Batch phosphate adsorption

An aqueous 100 mg/L stock solution of phosphate was prepared using anhydrous $K_3PO_4$, which acts as a model pollutant dissolved in double distilled water. The prepared solution was then diluted to desired concentrations (25, 50, and 100 mg/L). Batch experimentations were executed at 25 °C, with a shaking rate of 500 rpm. The suspensions were filtered via a 0.22 μm filter paper at different time intervals. The concentration of phosphate in an aqueous solution was measured using a UV–Vis spectrophotometer (TU-1810, Parsee, China) at $\lambda=690$ nm by the colorimetric method and through the ammonium molybdate–$SnCl_2$ method. All experiments were replicated three times, and the mean values were shown. The RE was estimated by using Equation (1):

$$RE = \frac{(C_0 - C_t)}{C_0} \tag{1}$$

where $C_0$ is the initial phosphate concentration (mg/L), at a time $t$, and $C_t$ denotes the $PO_4^{3-}$ concentration (mg/L).

The equilibrium adsorption capacity, $q_e$ (mg g$^{-1}$), was quantified by employing Equation (2):

$$q_e = \frac{V(C_0 - C_e)}{M} \tag{2}$$

where $C_e$ symbolizes the $PO_4^{3-}$ concentration (mg/L) at equilibrium, $V$ indicates the solution volume (L), and $M$ is the adsorbent mass used (g).

### 2.3.1. Effect of pH

In batch bottles, 50 mL of phosphate solutions (phosphate concentration 25 mg/L) and the nZVI adsorbent (560 mg/L dosage) were mixed. The pH value of the mixed solutions was changed to the preferred values from 2.0 to 12.0 due to the addition of HCl or NaOH solution. To ensure equilibrium, the sealed bottles were positioned in a thermostatic shaker (500 rpm) for 2 h at room temperature.

### 2.3.2. Influence of ionic strength and coexisting anions

To monitor the effect of ionic strength and coexisting anions on phosphate RE, the reactions were performed in the same manner as that of the above experiment. The addition of nZVI (560 mg/L) to 50 mL (25 mg/L) sample phosphate solution changing concentrations of NaCl (0.005–0.1 M) was done for establishing ionic strength dependence on phosphate removal. Likewise, coexisting anions such as carbonate and sulphate, which are commonly present in surface water and groundwater, were used for preparing 50 mL of phosphate solution. The concentrations of $CO_3^{2-}$ (0.05–0.2 M) and $SO_4^{2-}$ (0.05–0.2 M) were varied in the solution. The reaction was allowed for 2 h on a mechanical stirrer (500 rpm) at 25 °C, and the equilibrium phosphate concentrations were resolved at regular intervals.

### 2.3.3. Reusability test of nZVI

The nZVI adsorbent was collected after the adsorption experiment by centrifugation, washed thoroughly with double distilled water several times, and dried under vacuum. The dried nZVI adsorbent was further used for the removal of phosphates from the water samples when it was considered as the first reusability cycle. Here, the reusability of the adsorbent was checked by performing the experiment up to five cycles.

## 2.4. Real water sample collection

Real water samples were collected from Saheb bandh, Purulia district, in a polyethylene bottle of 5 L to perform the phosphate removal experiment. The water sample was well shaken before performing the reaction. The $PO_4^{3-}$ concentration in the real sample was determined by the ammonium molybdate method.

## 3. RESULT AND DISCUSSION

### 3.1. Structural and morphological studies

To investigate the phase constitution as well as the crystal structure of the synthesized nZVI, the XRD technique was employed. Figure 1 depicts the XRD patterns of the synthesized nZVI within the $2\theta$ range of 25°–75° plotted against the intensity of scattered rays.

In Figure 1, a broad peak was perceived at 44.8°, which may be the peak found due to the diffraction from the (110) plane due to the $\alpha$-phase of metallic iron (ICSD card no. code 98-002-1567) (Ghosh *et al.* 2017). Besides the above-mentioned peak, other peaks (marked with an asterisk) were also observed at 35.9° and 62.8°, which represent the formation of $Fe_3O_4$ and $Fe_2O_3$, respectively, on the exterior surface of the particles. The crystallite size of the synthesized nanoparticles was calculated using the Scherer equation [Equation (3)].

$$D = \frac{K\lambda}{\beta \cos\theta} \tag{3}$$

where $D$ denotes the average crystallite size, $\beta$ signifies the full width at half maximum (FWHM) of the diffraction peaks, $\theta$ symbolizes the Bragg angle, and $\lambda$ represents the wavelength of an X-ray source ($\lambda=0.15418$ nm) incident. The constant $K$ is associated with the shape of crystallite usually taken as 0.9, assuming spherical crystals (Langford & Wilson 1978). For nZVI, the crystallite size obtained from the Scherer equation is 12.83 nm.

Fig. S1(A) shows the nitrogen adsorption–desorption isotherms of synthesized nZVI particles. According to the IUPAC classification, the curve shows type IV isotherm, which indicates meso-porosity in nZVI. In this isotherm, the H3 type hysteresis loop reveals the existence of an irregular orientation of pores as well as interconnected slit-shaped pores in nZVI. The BJH pore size distributions (PSDs) derived from isotherm desorption data are shown in Fig. S1(B). The curve shows relatively wide PSDs in the mesoporous area. The textural properties of the synthesized nZVI are tabulated (Table S1).

Figure 2(a) and 2(b) depicts the FESEM image of synthesized nZVI. It was observed that the formed particles are spherical in shape with a dimension of about ~64 A°, which is due to the high viscosity of the solvent, i.e. glycerol. The reason behind this is that glycerol provides a definite shape and resists the oxidation of the nanoparticles during synthesis. Glycerol undergoes strong hydrogen bonding due to the presence of the poly-hydroxyl group and is therefore highly suitable for solvating the particles. This phenomenon restricts the growth of nZVI beyond a specific size and contributes to the flower-like morphology. The particles are agglomerated somewhere, which is clear from the FESEM image.

A group of chain-like particles (shown in Figure 3(a) and 3(b)) was formed due to the magnetic nature of the particles. A spherical-shaped structure was visible, which was formed by joining various petals like structures together. Figure 3(b)
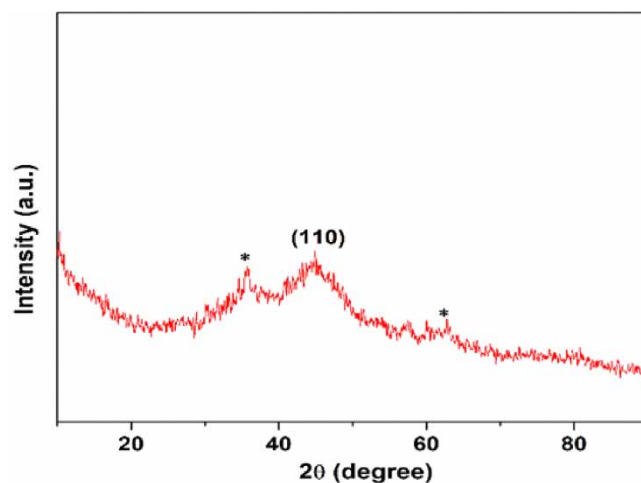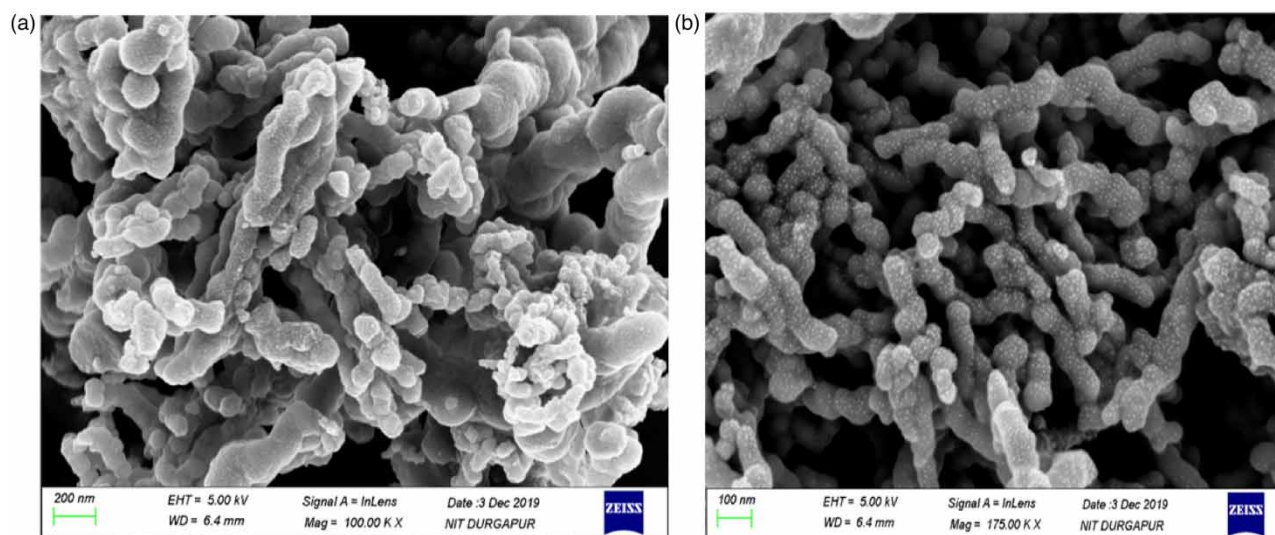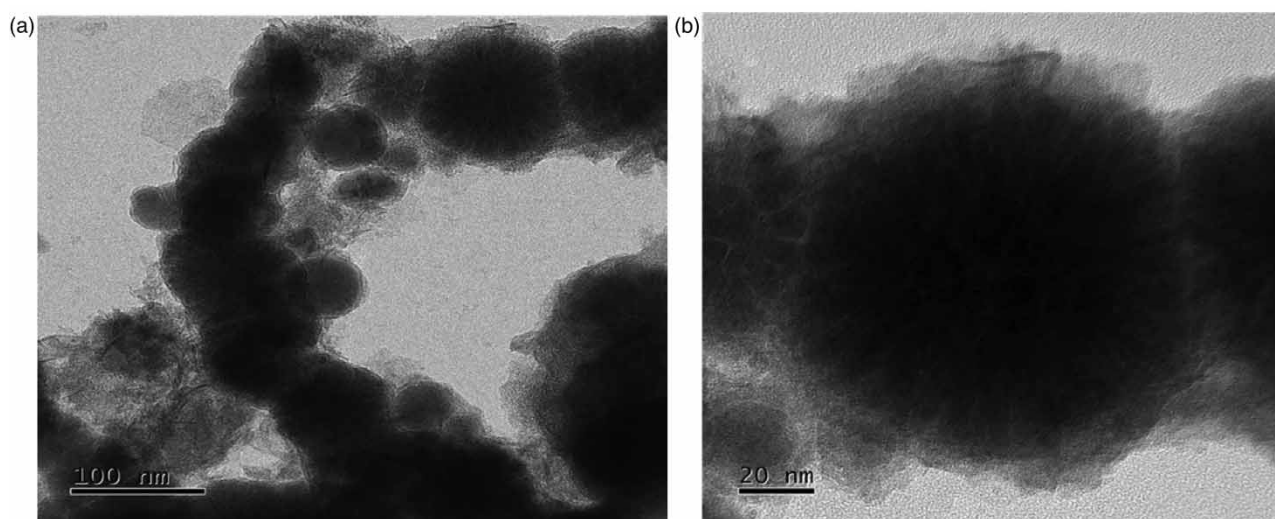


**Figure 1** | XRD patterns of nZVI.

**Figure 2** | (a) and (b) FESEM image of synthesized nZVI.



**Figure 3** | (a) and (b) HRTEM image of synthesized nZVI.

highlights a closer view of a single particle. Hence, it depicts that nZVI was enclosed by a thin layer-like substance. This may be ascribed to the existence of organic substances like glycerol adsorbed onto nanoparticle surfaces (Ghosh et al. 2019). The TEM image calculation of the particle size of nZVI showed an average particle of 50 nm.

Figure 4 demonstrates the characteristic EDX spectra, which show the presence of only iron and oxygen with no other impurities in the as-grown sample. Figure 5 shows the FT-IR spectrum of freshly prepared nZVI, which was recorded within the range of 4,000 and 400 $cm^{-1}$. Wide and solid peaks at $\sim$3,440 and $\sim$1,650 $cm^{-1}$ appeared due to the O–H stretching vibration and O–H bending vibration, respectively. This may be due to the presence of physiosorbed interstitial water atoms on the surface of nZVI (Wang & Zhang 1997). The band appeared at 1,425 $cm^{-1}$ due to the O–H bending vibration. This demonstrated the occurrence of surface hydroxyl groups on the surface of nZVI. It was observed that some peaks also appeared at 990, 698, and 446 $cm^{-1}$, which may be ascribed to the lattice vibrations that originated from Fe–O–Fe and Fe–O iron–oxygen bonds (Ai et al. 2008; Zhou et al. 2011).
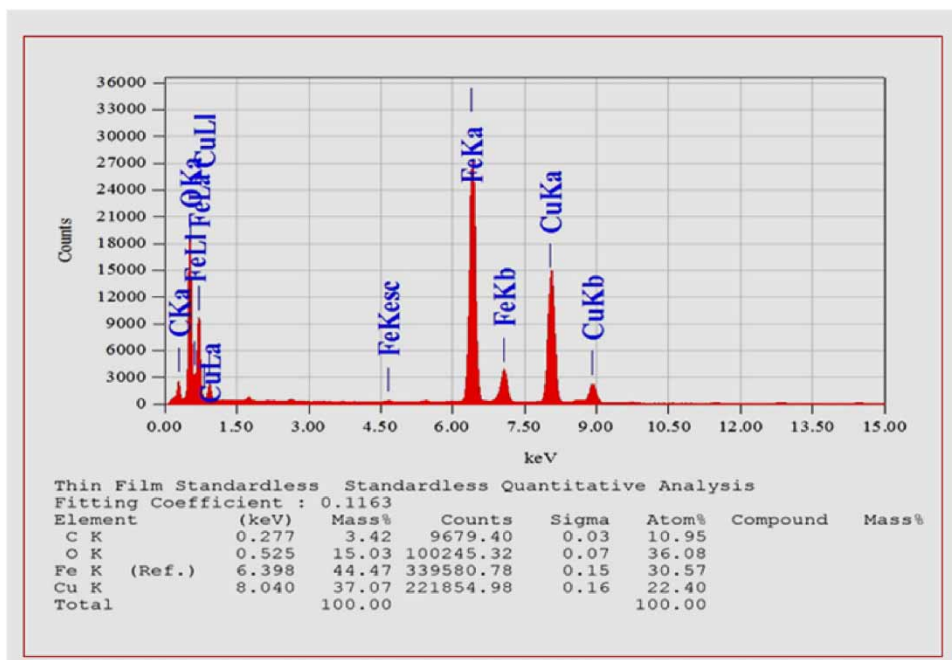
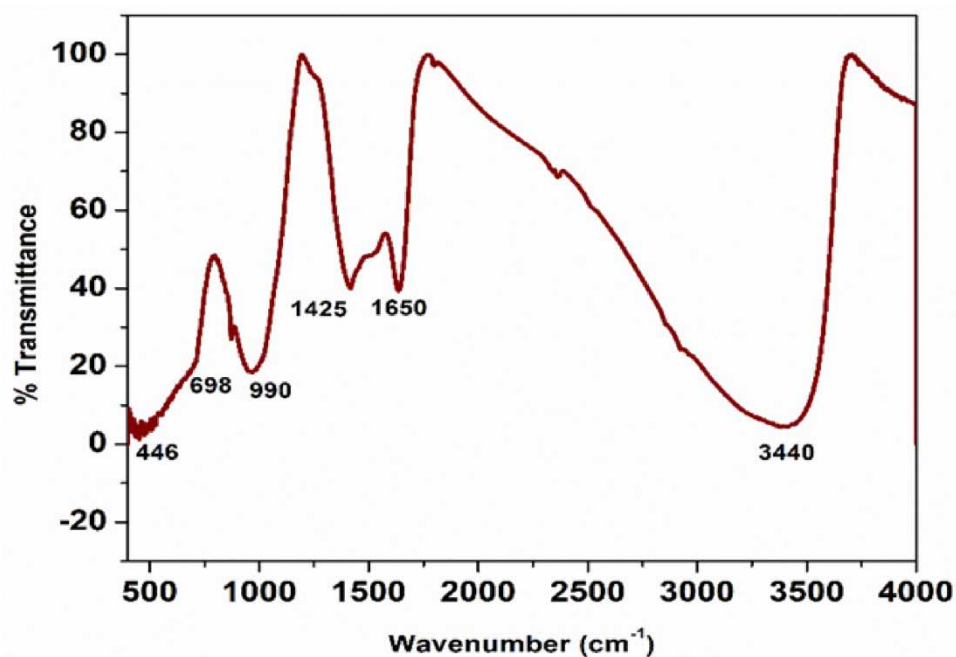**Figure 4** | Characteristic EDX spectra of synthesized nZVI.



**Figure 5** | FT-IR spectra of fresh nZVI.

## 3.2. Phosphate remediation from laboratory-based water

Different factors such as initial phosphate concentration, the dosage of adsorbent (nZVI), pH, ionic strength, and coexisting anions influencing the phosphate RE from laboratory-based synthesized water were studied efficiently and elaborated in this section.

### 3.2.1. Effect of adsorbent dosage

The adsorbent dose is regarded as one of the crucial parametric quantities that influence the adsorption method. Herein, $PO_4^{3-}$ RE (%) increases strongly with increasing the nZVI dose from 140 to 280 mg/L at pH 2, an initial $PO_4^{3-}$ concentration of 25 mg/L, and a contact time of 120 min, as represented in Figure 6. Afterward, $PO_4^{3-}$ RE (%) gradually increases with a subsequent increase in the adsorbent dose. Maximum $PO_4^{3-}$ RE is achieved at an adsorbent dose of 560 mg/L. It is observable that the number of active sites surges with increasing the adsorbent dose. Hereafter, an increment of $PO_4^{3-}$ RE (%) is obtained as a final outcome (Fu & Quan 2006). Above the dosage of 560 mg/L nZVI, an improvement in $PO_4^{3-}$ RE (%) is not observed due to the tendency of nZVI to agglomerate. Thus, the length of diffusion paths is enhanced, and hence, $PO_4^{3-}$ molecules can easily diffuse into the pores because of their developed higher mass transfer resistance (Meena *et al.* 2005). Another important parameter influencing phosphate removal from aqueous solution is contact time. This can be perceived in the following way: $PO_4^{3-}$ RE (%) increases when the contact time increases from 100 to 120 min, but when the contact time increases again up to a certain limit, $PO_4^{3-}$ RE (%) remains unchanged. Furthermore, $PO_4^{3-}$ RE (%) increases with increasing the contact time. This is due to the adsorbent taking more time to adsorb $PO_4^{3-}$ molecules. On the other hand, the $PO_4^{3-}$ RE (%) value remains unchanged or decreases with a further increase in contact time as the desorption of $PO_4^{3-}$ ions occurs from the adsorbent.

### 3.2.2. Effect of initial phosphate concentration

The changes in $PO_4^{3-}$ RE (%) with the variation of initial $PO_4^{3-}$ concentration within the range of 25–100 mg/L can be represented in Figure 7, where the pH is the actual pH of $PO_4^{3-}$ spiked synthetic water (pH 6, without the addition of any acid or base), the nZVI dose at 560 mg/L, and the contact time at 120 min. It is shown from Figure 7 that the highest % RE of 90% is obtained at an initial $PO_4^{3-}$ concentration of 25 mg/L, while above 25 mg/L, $PO_4^{3-}$ RE (%) becomes lower. At 50 and 100 mg/L of initial $PO_4^{3-}$ concentrations, the % $PO_4^{3-}$ REs are obtained to be 71.1 and 38.4%, respectively, at 120 min, which are much lower than the 25 mg/L initial $PO_4^{3-}$ concentration. This is probably due to the fact that all available active sites of the adsorbent are filled with $PO_4^{3-}$ ions at a fixed nZVI dosage. Hence, a further increase in the $PO_4^{3-}$ concentration in this saturated condition results in overcrowding in the system, which ultimately results in lower $PO_4^{3-}$ RE (%) (Garg *et al.* 2004).

### 3.2.3. Effect of initial pH

The initial pH of an aqueous solution is a basic parameter that is greatly involved in the adsorption of cations and anions at the solid–liquid boundary. Herein, the variation of phosphate RE was examined by varying the pH of the reaction medium at 2, 6, 8, 10, and 12, keeping the initial phosphate concentration and the nZVI dosage of 25 and 560 mg/L, respectively. In this case, increasing pH values from 2 to 12 led to a monotonically decreased $PO_4^{3-}$ RE from 96 to 22.4% (Figure 8). When the solution pH was set to 2, several $H^+$ ions prevailed in the reaction medium. These $H^+$ ions protonated the adsorbent surface
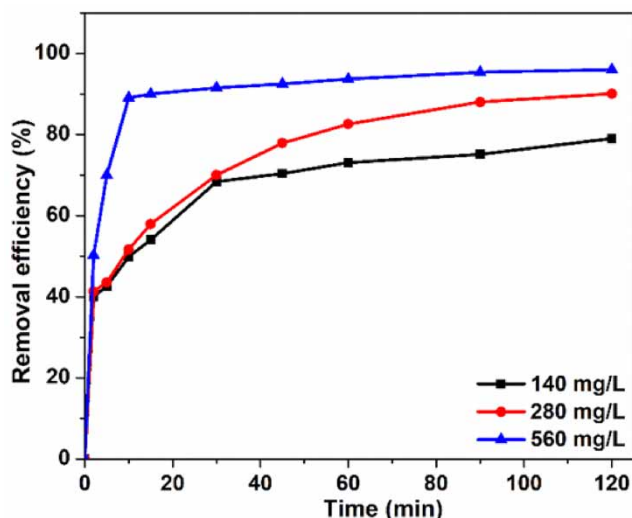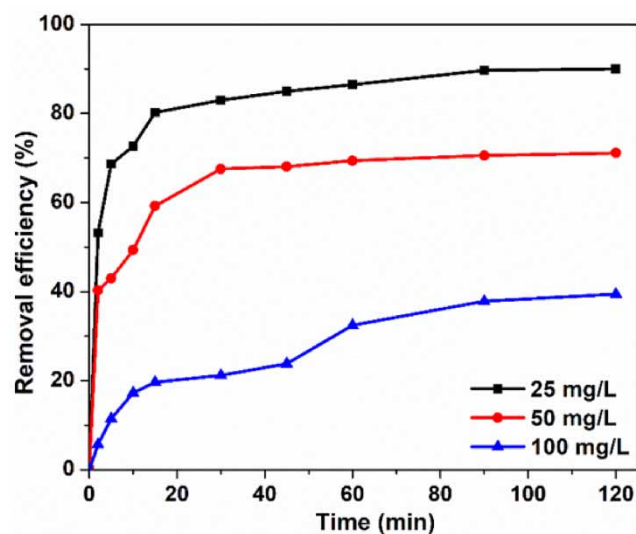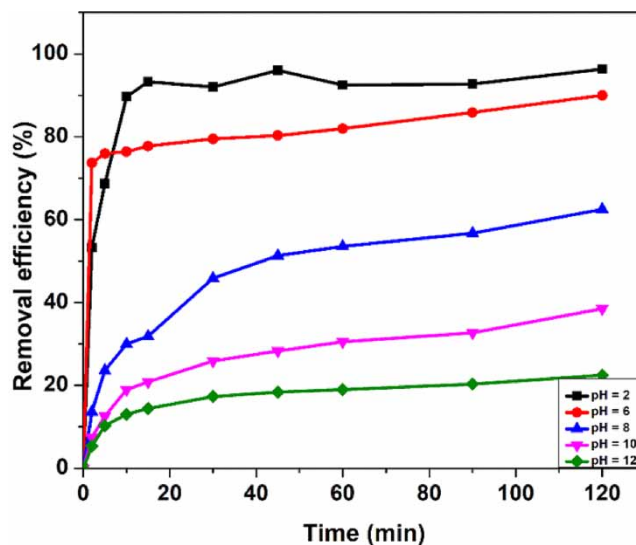


**Figure 6** | Phosphate RE (%) vs. time (mint) plot with a varying dose of nZVI.

**Figure 7** | $PO_4^{3-}$ RE (%) vs. time (min) plot with a varying initial concentration of $PO_4^{3-}$.



**Figure 8** | Effect on initial pH on phosphate removal (%) with time.

significantly. Thus, the negatively charged $PO_4^{3-}$ ions could be easily adsorbed on the protonated nZVI surface by electrostatic attraction at pH 2. Herein, when the solution pH was in the range of 2–6, the dominant species of phosphate in the solution was $H_2PO_4^-$. Therefore, a competition between $H_2PO_4^-$ and $PO_4^{3-}$ for getting adsorbed on the nZVI surface occurred, which resulted in a reduction of RE from 96 to 90%. Moreover, this phenomenon can also be elucidated on the basis of the isoelectric point (IEP), i.e. ~8.0 of the synthesized nZVI (Banerjee *et al.* 2016). It is clear from its IEP value that nZVI possesses a higher surface positive charge when the solution pH becomes less than that of IEP, which leads to the strong electrostatic attraction between $PO_4^{3-}$ and the nZVI surface. Meanwhile, the dominant species of phosphate in the solution changes to $HPO_4^{2-}$ above pH 6, which has a stronger negative charge than $H_2PO_4^-$. The generated strong coulomb repulsive interaction between the negatively charged nZVI surface and $HPO_4^{2-}$ as well as the competition between $HPO_4^{2-}$ and $PO_4^{3-}$ can largely degrade the phosphate adsorption performance. However, at pH 10 and 12 (a highly alkaline medium), deprotonation of

nZVI invokes the electrostatic repulsive interaction between the anionic $PO_4^{3-}$ and the negatively charged nZVI surface, resulting in a reduction of phosphate adsorption. Besides this, ample $OH^-$ ions compete with $PO_4^{3-}$ ions to be adsorbed on the nZVI surface, which leads to a decrease of $PO_4^{3-}$ RE of synthesized nZVI (Sun *et al.* 2007; Wu *et al.* 2013a, 2013b). On the other hand, the coagulation or precipitation method most likely plays a vital role. During the $PO_4^{3-}$ removal reaction synthesized by nZVI, some portions of nZVI may be oxidized to Fe(II) or Fe(III). Some researchers have also reported that the *in-situ*-generated Fe(III) possesses an excellent affinity for phosphate through chemical precipitation owing to its higher positive charge (Li *et al.* 2009; An *et al.* 2014). In this case, at acidic, neutral, or basic pH, $PO_4^{3-}$ removal occurs easily through the formation of $FePO_4$ or $Fe_3(PO_4)_2$ precipitate in an aqueous solution. Thus, the *in-situ*-generated Fe(III) or Fe(II) in solution is combined with phosphate easily to form precipitates, which leads to efficient $PO_4^{3-}$ removal (Fytianos *et al.* 1998). In this way, chemical precipitation plays a vital role in $PO_4^{3-}$ removal. Additionally, Fig. S2 depicts the bar diagram that shows the variation of phosphate concentrations at pH values of 2, 6, 8, 10, and 12 with specific concentrations of 25 mg/L initial $PO_4^{3-}$ and 560 mg/L nZVI. The diagram reveals an improved $PO_4^{3-}$ removal of 96% under acidic environments.

### 3.2.4. Effect of the shaking rate

The influence of the shaking rate on the adsorption of $PO_4^{3-}$ from the aqueous solution was studied by keeping the initial $PO_4^{3-}$ concentration of 25 mg/L and the nZVI dosage of 560 mg/L at pH 2 under different shaking rates of 100, 200, 300, 400, and 500 rpm. Figure 9 reveals that $PO_4^{3-}$ RE increases with increasing the shaking rate from 100 to 500 rpm. With the increase in the shaking rate, the rate of diffusion of the $PO_4^{3-}$ ions from the bulk liquid to the liquid boundary layer surrounding the nZVI particles becomes higher because of an enhancement of the turbulence and a decrease in the thickness of the liquid boundary layer. In addition, this effect may be enhanced by the greater fragmentation of the adsorbent particles, which accompanies the increased shaking rate. Hence, an improved $PO_4^{3-}$ RE of 96% was observed at a higher shaking rate of 500 rpm. However, above 500 rpm shaking rate, no significant increase in the $PO_4^{3-}$ RE was obtained (Priddy & Hanley 2003; Shiau & Pan 2004; Ihsanullah *et al.* 2015). This is due to the fact that at a very high shaking rate, the kinetic energies of both the adsorbate molecules ($PO_4^{3-)}$ and the adsorbent particles (nZVI) increase to such an extent that they collide with each other, hastily resulting in a detachment of the loosely bound adsorbate molecules ($PO_4^{3-}$).

### 3.2.5. Influence of ionic strength and coexisting anions

Several coexisting anions present in wastewater along with phosphate and having their influence on phosphate removal were studied. The salts of chloride, sulphate, and carbonate with their varying concentrations in phosphate solution were set for the batch reaction discussed earlier, and the phosphate removal was investigated as shown in Fig. S3. The results from Fig S3(A)
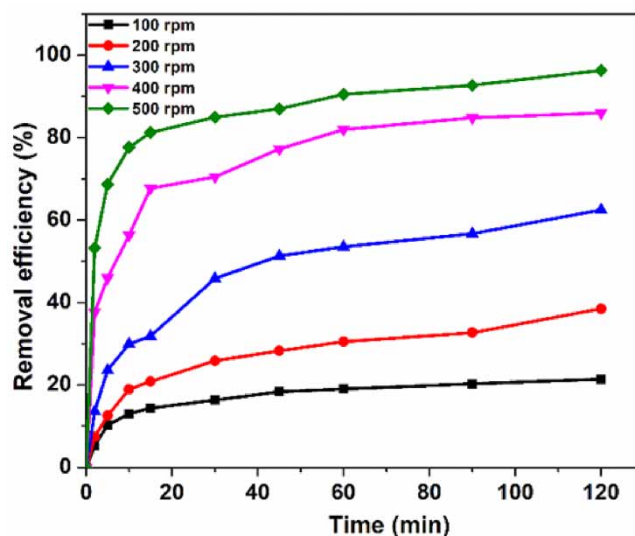


**Figure 9** | Effect of the shaking rate on phosphate removal (%) with time.

show that the presence of 0.005 M NaCl yields a phosphate removal of 95.53% at lower pH, while the presence of 0.01 moles of $Na_2SO_4$ shows a phosphate removal of 94.53% (Fig S3(B)). This shows that the existence of these common anions does not disturb the removal of phosphate by nZVI; however, $CO_3^{2-}$ strongly affects $PO_4^{3-}$ adsorption, and the % of $PO_4^{3-}$ removed in our experiment was 31.29, 25.09, and 17.06% at 0.0025, 0.005, and 0.01 mole concentrations, respectively (Fig S3(C)) (Wu et al. 2013a, 2013b; Zhang et al. 2017). Herein, the anions forming the outer sphere complexes are strongly dependent on ionic strength, which may be due to the electrostatic forces. In this case, phosphate probably forms inner sphere complexes via ionic bonding at the solid–liquid boundary, which is quite stable compared to outer sphere complexes (Liu et al. 2007).

Here, we present Table S2 containing comparative data for the removal of $PO_4^{3-}$ contaminant from water samples by various research groups.

### 3.2.6. Adsorption kinetics

A determination of the kinetics of the process is essential in order to find the industrial application of any process. Meanwhile, required design information such as the time required for performing a single batch, the size of the apparatus, etc., can be established with the help of a kinetic study. The kinetic parameters of adsorption processes can be evaluated from several well-known kinetic models. In our case, the obtained experimental data were fitted into several in-built models such as pseudo-1st-order, pseudo-2nd-order, and Elovich models. The linear forms of the pseudo-1st-order (Simonin 2016) and pseudo-2nd-order models (Gao et al. 2019) can be articulated via Equations (4) and (5), respectively.

$$\log (q_e - q_t) = \log q_e - \frac{k_f \; t}{2.303} \tag{4}$$

$$\frac{t}{q_t} = \frac{1}{k_s q_e^2} + \frac{t}{q_e} \tag{5}$$

where $q_e$ and $q_t$ signify the adsorption capacity (mg g$^{-1}$) of nZVI remaining in equilibrium and at time $t$ (s), respectively. $k_f$ and $k_s$ are pseudo-1st-order rate constant (s$^{-1}$) and pseudo-2nd-order rate constant (g mg$^{-1}$ s$^{-1}$), respectively.

Equation (6) signifies the linear form of the Elovich model, which is a well-known method to demonstrate the kinetics of the chemisorption process.

$$q_t = \frac{1}{\beta} \ln (\alpha \beta) + \frac{1}{\beta} \ln (t) \tag{6}$$

where $q_t$ symbolizes the adsorption capacity (mg g$^{-1}$) of nZVI at time $t$ (s), and $\alpha$ and $\beta$ indicate the rate of chemisorption (mg/L s$^{-1}$) at zero coverage and the desorption constant (g mg$^{-1}$), associated with surface analysis and activation energy analysis for chemisorption, respectively (Chen et al. 2010). The values of $\alpha$ and $\beta$ can be obtained by plotting $q_t$ vs. ln($t$) [Equation (6)].

The duration of contact time for adsorption was altered to acquire the kinetic data, while the rest of the parametric quantities such as initial phosphate concentration, adsorbent dose, and pH remained constant at 25, 560, and 2 mg/L, respectively. In Figure 10, pseudo-1st-order, pseudo-2nd-order, and Elovich models were implemented to the experimental data having $R^2$ values of 0.0882, 0.9996, and 0.7041. Based on the $R^2$ value, it is supposed that the pseudo-2nd-order model possessing a higher correlation coefficient ($R^2 = 0.9996$) facilitates the process of $PO_4^{3-}$ adsorption. This result suggests that the process of $PO_4^{3-}$ adsorption can be governed via the chemisorption process (Wang et al. 2016; Yuan et al. 2018). Thus, chemical interactions between the adsorbent and the adsorbate occur as the adsorption follows pseudo-second-order kinetics. The constant $k_s$ was 0.03010 g mg$^{-1}$ s$^{-1}$, and the measured adsorption capacity at equilibrium (42.37 mg g$^{-1}$) was close to the investigational value. The parameters regarding various kinetic models are summarized in Table S3.

### 3.2.7. Adsorption isotherm

In our study, the equilibrium data were fitted into some in-built isotherm models such as the Langmuir, Freundlich, and Temkin isotherm models. The Langmuir [Equation (7)], Freundlich [Equation (8)], and Temkin isotherm [Equation (9)]
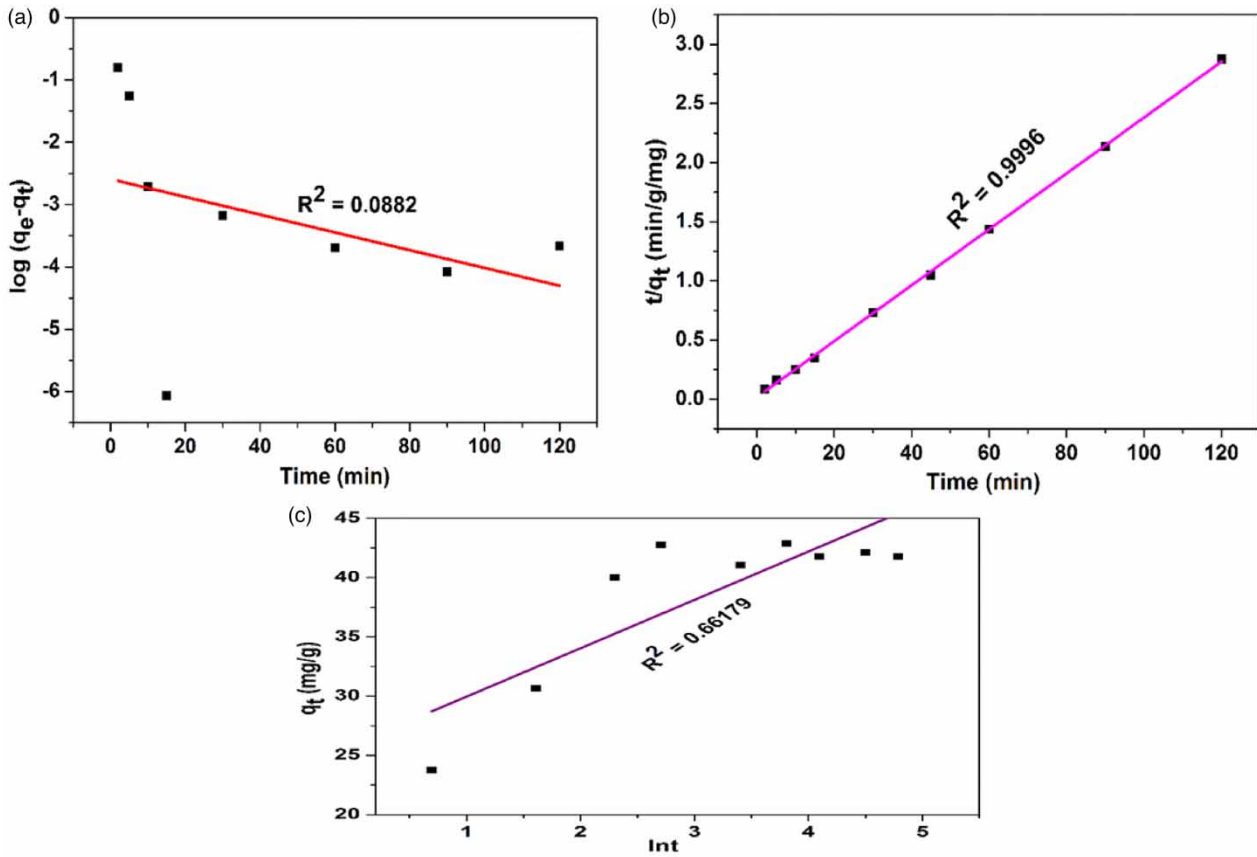
**Figure 10** | Adsorption kinetic studies of $PO_4^{3-}$ removal: (a) pseudo-1st-order model; (b) pseudo-2nd-order model, and (c) the Elovich model.

models were fitted to data collected from adsorption isotherms.

$$\frac{C_e}{q_e} = \frac{C_e}{q_m} + \frac{1}{K_L q_m} \tag{7}$$

$$\ln q_e = \ln K_F + \frac{1}{n} \ln C_e \tag{8}$$

$$q_e = \frac{RT}{b} \ln K_T + \frac{RT}{b} \ln C_e = B_1 \ln K_T + B_1 \ln C_e \tag{9}$$

where $C_e$ represents the $PO_4^{3-}$ equilibrium concentration (mg/L), $q_e$ and $q_m$ denote the equilibrium and maximum adsorption capacity (mg g$^{-1}$), $K_L$ (L mg$^{-1}$), and $K_F$ signifies the constants of adsorption for the Langmuir and Freundlich models. $1/n$ is a constant of nonlinearity. Equation (10) was employed to calculate the parameter $R_L$ of equilibrium.

$$R_L = \frac{1}{(1 + K_L C_0)} \tag{10}$$

where $C_0$ signifies the highest initial concentration of phosphate (mg/L), and $K_L$ is the Langmuir adsorption constant (L mg$^{-1}$).

In Equation (8), $K_T$ and $b$ signify the equilibrium-binding constant (L mg$^{-1}$) and adsorption energy (J mol$^{-1}$), respectively, and $R$ and $T$ indicate the universal gas constant (J mol$^{-1}$ K$^{-1}$) and temperature (K), respectively. Here, $K_T$ and $b$ can be calculated by plotting $q_e$ vs. ln $C_e$ in a graph.

The correlation between the amount of adsorbate adsorbed per unit weight of adsorbent ($q_e$, mg g$^{-1}$) and the concentrations of adsorbate in the bulk solution ($C_e$, mg/L) at a certain temperature under equilibrium environments is established from an adsorption isotherm. They are very beneficial in furnishing evidence about adsorption mechanisms, surface properties, and attraction of an adsorbent toward an adsorbate (Vijayakumar et al. 2010). Adsorption experiments were done at various initial $PO_4^{3-}$ concentrations, at a constant pH 2, in the presence of 560 mg/L adsorbent dosage and 120 min contact time. Figure 11 reveals the measured experimental data that were fitted into the Langmuir, Freundlich, and Temkin isotherm models. The $R^2$ values achieved using the Langmuir, Freundlich, and Temkin and Redlich–Peterson isotherm models are 0.9525, 0.9437, and 0.9912, respectively. Therefore, the highest $R^2$ value achieved for $PO_4^{3-}$ removal via the nZVI adsorbent indicated that the adsorption follows the Temkin isotherm model. The maximum adsorption capacity ($q_m$) obtained from the Temkin model was 140.84 mg g$^{-1}$. The parametric quantities for the various isotherm models are précised in Table S4. Therefore, according to the significance of the Temkin isotherm, the adsorption heat of all $PO_4^{3-}$ ions decreases linearly with the increase in the coverage of the nZVI surface. This type of adsorption is characterized by a uniform distribution of binding energies up to a maximum binding energy (Piccin et al. 2011).

### 3.2.8. Adsorption thermodynamics

To understand the effect of temperatures on the reaction, thermodynamic parameters such as entropy change ($\Delta S^o$) and enthalpy change ($\Delta H^o$) were derived at different temperatures. The energy of activation for the adsorption of phosphate on nZVI can be determined by the second-order rate constant expressed in the Arrhenius (Najafi et al. 2015) equation

$$\ln k_2 = \ln k_0 - E/RT \tag{11}$$
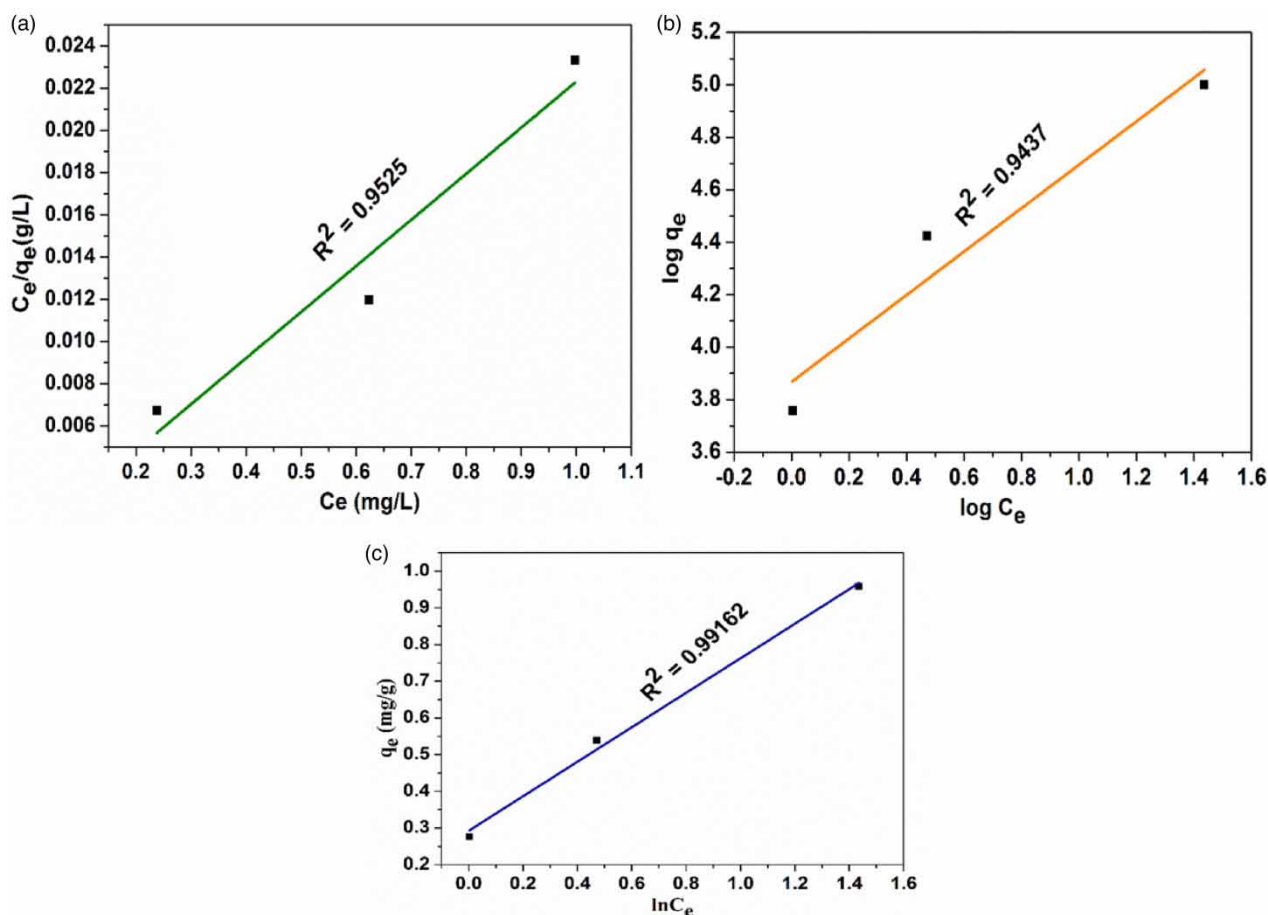


Figure 11 | Adsorption isotherm experiments of $PO_4^{3-}$ removal using (a) Langmuir isotherm, (b) Freundlich isotherm, and (c) Temkin isotherm.

where $k_0$ is the constant of the equation (g mg$^{-1}$ min$^{-1}$), $E$ is the energy of activation (J mol$^{-1}$), $R$ is the gas constant (8.314 J mol$^{-1}$ K$^{-1}$), and $T$ is the temperature in kelvin. The free energy change is obtained using the following equation:

$$\Delta G = -RT\ln K_c \tag{12}$$

where $\Delta G^o$ is the free energy (kJ mol$^{-1}$), $K_c$ is the equilibrium constant, $R$ is the universal gas constant, and $T$ is the temperature in kelvin. Other thermodynamic parameters such as entropy change ($\Delta S^o$) and enthalpy change ($\Delta H^o$) were determined using the Van't Hoff equation

$$\ln K_c = \frac{\Delta S}{R} + \frac{\Delta H}{RT} \tag{13}$$

The energy ($E$) value was 9.6792 kJ mol$^{-1}$ calculated from the slope of the fitted Equation (10). The values of $K_c$ and $\Delta G^o$ are tabulated (Table 1). The enthalpy change ($\Delta H^o$) and the entropy change ($\Delta S^o$) of phosphate adsorption on nZVI are 9.3457 kJ mol$^{-1}$ and 0.03134 J mol$^{-1}$ K$^{-1}$, respectively, which are achieved from the slope and intercept values of the Van't Hoff linear plots of ln$K_c$ vs. $1/T$ (Figure 12(b)). The endothermic nature of this adsorption process is confirmed from the positive value of enthalpy change ($\Delta H^o$), and the negative value of change in internal energy ($\Delta G^o$) shows the spontaneous adsorption of PO$_4^{3-}$ on nZVI (Kamaraj *et al.* 2016). Positive values of entropy change are a clear indication of increased randomness of the solution interface during the adsorption of PO$_4^{3-}$ on nZVI (Table 1). The expansion of pore

**Table 1** | Thermodynamic parameter for the adsorption of PO$_4^{3-}$ on nZVI

| Temperature (K) | $K_c$ | $\Delta G^o$ (kJ mol$^{-1}$) | $\Delta H^0$ (kJ mol$^{-1}$) | $\Delta S^0$ (J mol$^{-1}$ K$^{-1}$) |
|---|---|---|---|---|
| 303 | 1.00008 | −0.20 | 9.3457 | 0.03134 |
| 313 | 1.00017 | −0.44 | | |
| 323 | 1.00028 | −0.75 | | |
| 333 | 1.00039 | −1.08 | | |
| 343 | 1.00050 | −1.42 | | |
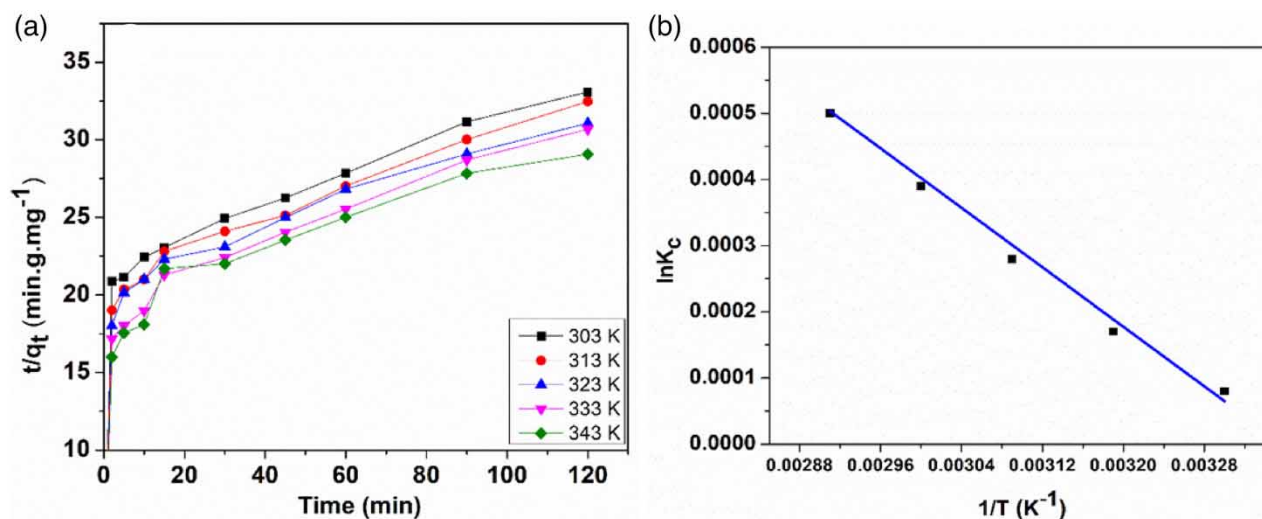


**Figure 12** | (a) Second-order kinetic model plot. (b) Plot of ln$K_c$ vs. $1/T$ at different temperatures (303–343 K).

size and the activation of the nZVI surface occur at higher temperatures, which ultimately results in increasing the adsorption capacity.

## 3.3. Possible mechanism

The probable mechanism behind the removal of phosphate from water is represented in Figure 13.

The corrosion of the electron donor and the nZVI core results in the release of $Fe^{2+}$ and $Fe^{3+}$ ions. Furthermore, the ferrihydrite (FeOOH) sorption passive layer is formed following the reactions shown below (Dolatabadi & Ahmadzadeh 2019).

$$2Fe^0 + 4H^+ + O_2 = 2Fe^{2+} + 2H_2O$$

$$2Fe^{2+} + 2H_2O = 2Fe^{3+} + 2H_2 + 2OH^-$$
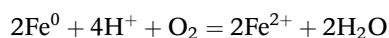
Then, the soluble $PO_4^{3-}$ (sorbate) is diffused from the bulk solution to the outer plane around nZVI (sorbent) via liquid–liquid diffusion. A feasible adsorption of the sorbate solute on to the active sites on the outer surface of nZVI occurs. The liquid–solid step occurs mainly through both physisorption and chemisorption to control this step.

(1) **Physisorption:** The electrostatic attraction between the negatively charged phosphate ($PO_4^{3-}$) species and the positively charged nZVI surface results in the deposition of iron phosphate.

$$FeOOH + PO_4^{3-} \rightarrow FeOOH = PO_4$$
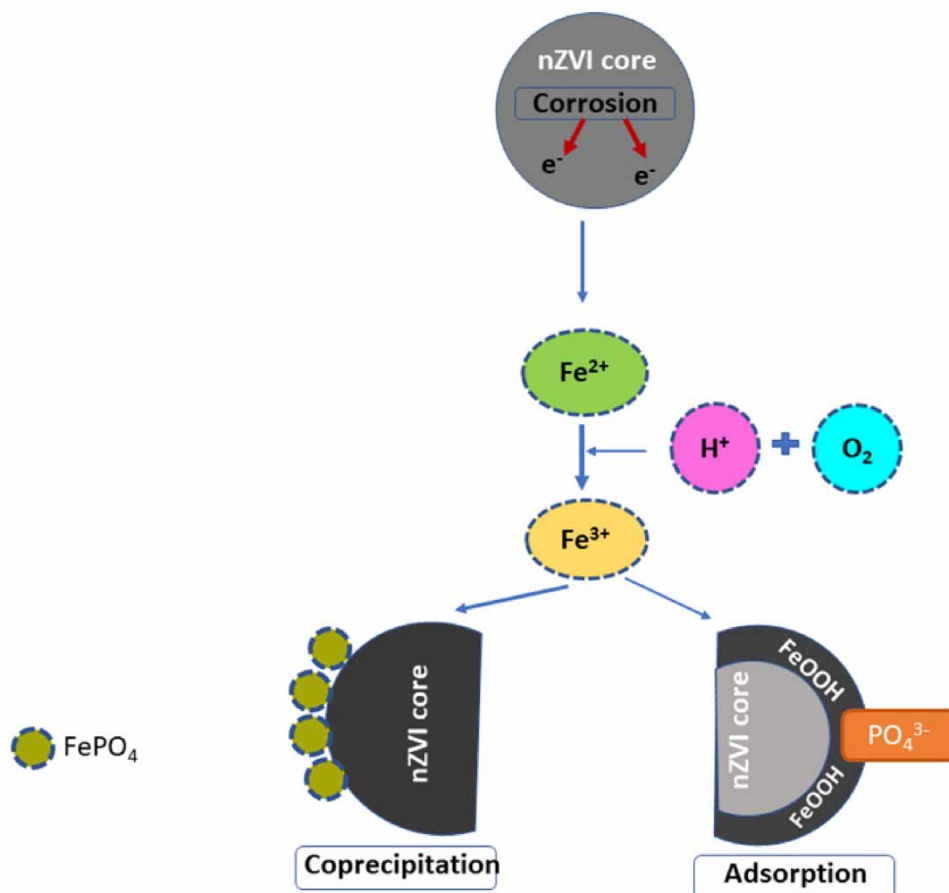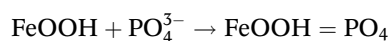


**Figure 13** | Plausible schematic mechanism of phosphate removal by nZVI.

(2) **Chemisorption:** The coprecipitation of the released iron oxides ($Fe^{2+}/Fe^{3+}$) with $PO_4^{3-}$ on to the nZVI surface occurs via chemisorption.

$$Fe^{2+} + PO_4^{3-} \rightarrow Fe_3\{PO_4\}_2$$

$$Fe^{3+} + PO_4^{3-} \rightarrow FePO_4$$
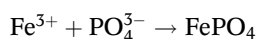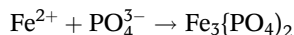
FT-IR spectra of nZVI before phosphate adsorption and after adsorption were compared for the identification of the interaction between nZVI and phosphate during the adsorption process. According to Figure 14, a broad band appears at $3,440\ cm^{-1}$, indicating the presence of coordinated water molecules, and the peak remains almost unchanged before and after phosphate adsorption. This shows that the physically adsorbed $H_2O$ molecules do not take part in the phosphate adsorption process. After adsorption, the bands at 870 and $1,425\ cm^{-1}$, assigned to the bending vibration peak of the surface water hydroxyl and hydroxyl groups of nZVI, respectively, disappear (Li *et al.* 2017). On the other hand, another hydroxyl group band at $982\ cm^{-1}$ weakens, signifying that the surface hydroxyl groups might be substituted by adsorbed phosphate. No new peaks generated from the vibration of P–O bonds develop after the uptake of phosphate due to the overlap between the vibration of P–O bonds and the hydroxyl groups of nZVI. This result proves that substitution occurs, which leads to the coprecipitation of iron phosphate.

### 3.3.1. Reusability test of nZVI

It can be well understood that any heterogenous adsorbent material will prove valuable for industrial or large-scale applications if it is suitable for reusability. In this context, to check the probability of the prepared nZVI adsorbent to treat large-scale pollutant water samples batchwise, we performed a reusability test of the adsorbent by fixing the dosage of the
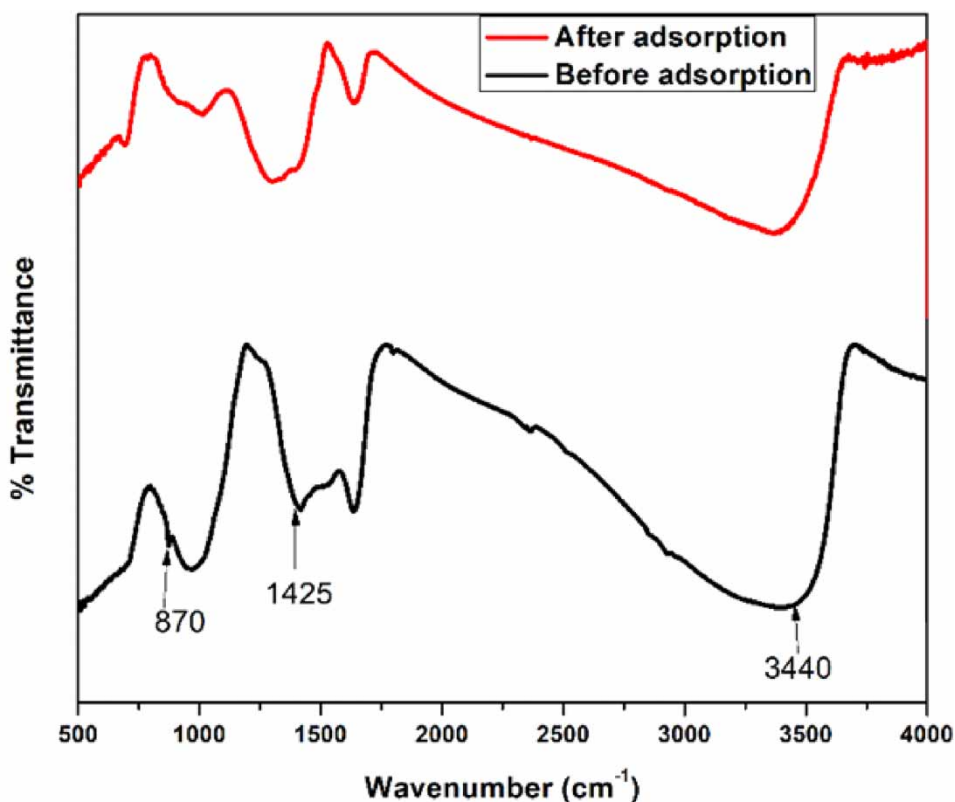


**Figure 14** | FT-IR spectra before and after the adsorption of phosphate by nZVI.
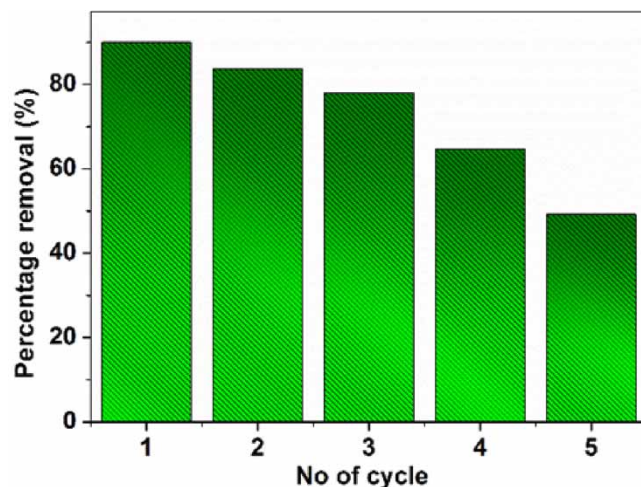
**Figure 15** | Reusability study of nZVI.

recovered nZVI nanoparticle at 560 mg/L and at a $PO_4^{3-}$ concentration of 25 mg/L (shown in Figure 15). All the reactions were continued for 2 h at 25 °C, i.e. under the same experimental condition. From Figure 15, it is evident that the phosphate RE by the recovered adsorbent, nZVI, is quite effective (>80% removal) up to three cycles. However, the RE drastically decreases in the fourth cycle, even dropping to 50% in the fifth cycle. This drop in RE must be explained by the fact that water samples contain an appreciable amount of dissolved oxygen, which leads to the oxidation of nanoscale iron particles when exposed in a reaction medium several times (Siddiqi & Chandrasekhar 2010). Long exposures, even in several steps, lead to the growth of an iron oxide layer over the iron nanosurface, decreasing its surface area. Thus, the efficiency of the adsorbent drops sharply.

Water samples from the Saheb Bandh Lake were tested for various parameters such as pH, Chemical oxygen demand (COD), Biological Oxygen Demand (BOD), Electrical Conductivity (EC), temperature, Dissolved oxygen (DO), Total Dissolved Solids (TDS), and total hardness, and their values are tabulated (Table S4).

## 4. APPLICATIONS

To evaluate the potentiality of the synthesized adsorbent, i.e., nZVI for practical application, real water samples were collected from Saheb Bandh and treated using the synthesized nZVI. Before treating the collected lake water, several important characteristics were determined, which are listed below (Table 2).

### 4.1. Phosphate removal from real water samples

Herein, we utilized a laboratory-based cost-effective method to synthesize nanoscale zerovalent iron (nZVI) and evaluated its feasibility as an adsorbent toward achieving clean and hygienic water by removing phosphate contaminants present in real water samples.

#### 4.1.1. Phosphate removal study based on time

At first, phosphate removal study from Bandh water was conducted at room temperature by keeping the nZVI dosage at 560 mg/L and at a neutral pH. From Fig S4, it can be understood that with increasing the time of reaction $PO_4^{3-}$, the removal percentage increases rapidly. The phosphate RE reaches about 86.5% at 120 min reaction time. The scope of $PO_4^{3-}$ to be adsorbed on the nZVI surface gradually increases with increasing the reaction time as nZVI took more time to adsorb in the Bandh (real) water solution. But above the 120 min reaction time, phosphate RE is unaltered because all the adsorbed sites or pores of nZVI become full with $PO_4^{3-}$.

#### 4.1.2. Effect of pH variation

The influence of pH on $PO_4^{3-}$ removal from Saheb Bandh water was carried out by keeping the pH range from 2 to 10 and the nZVI dosage at 560 mg/L. From Fig. S5, it is clear that the % RE becomes lower at pH 10 and reaches about only 50%. But

**Table 2** | Values of different parameters of Saheb Bandh Lake water, Purulia

| S. No. | Parameters | Obtained values |
|---|---|---|
| 1 | Temperature | 20.4 °C |
| 2 | pH | 7.4 |
| 3 | Electrical conductivity | 420 μS cm$^{-1}$ |
| 4 | Total dissolved solids | 192 mg/L |
| 5 | Dissolved oxygen | 6.8 mg/L |
| 6 | Biochemical oxygen demand | 4.32 mg/L |
| 7 | Chemical oxygen demand | 160 mg/L |
| 8 | Total hardness | 172 mg/L |
| 9 | Turbidity | 5–10 NTU |
| 10 | DOC | 0.8 mg/L |
| 11 | TOC | 4.5 mg/L |
| 12 | Total phosphorous (TP) | 26.368 mg/L |
| 13 | Total Kjeldahl Nitrogen (TKN) | 0.0–4.48 mg/L |
| 14 | $NO_3$-N | 0.88 mg/L |
| 15 | $NH_4$-N | 0.4 mg/L |
| 16 | p-alkalinity | Nil |
| 17 | m-alkalinity | 155.53 mg/L |
| 18 | $PO_4$-P | 25.67 mg/L |

the % RE is maximum (99%) at pH 2. Finally, the % RE reaches nearly 90% at pH 6. At a lower pH, phosphate is mainly present in the form of $H_3PO_4^-$ and $H_2PO_4^-$, while at a pH above 10, phosphates are mainly present in the form of $PO_4^{3-}$. These results can be studied on the basis of the IEP of the nZVI particles, which is ~8.0. Therefore, the nZVI surface possesses a more positive charge when the pH of the solution is less than that of the IEP. Hence, the absorption of negatively charged species is better at a lower pH compared with that in highly basic pH conditions. The affinity of nZVI toward phosphate ions decreases at a higher pH because of the presence of ample $OH^-$ ions, which compete for the adsorption sites along with $PO_4^{3-}$ ions.

## 5. COST ANALYSIS

The cost-effectiveness factor of the remediation process is a crucial parameter to establish the field application feasibility of synthesized nZVI. The total cost calculation for the laboratory preparation of 1 g of nZVI is represented in Table S4. From Table S4, it is clear that the cost incurred for the preparation of the adsorbent is approximately INR 125.478 g$^{-1}$.

## 6. CONCLUSION

In summary, spherical-shaped nZVI was successfully synthesized by the reduction method, and this nZVI was employed for the removal of phosphate from laboratory-based synthetic water as well as real water collected from Saheb Bandh, Purulia, West Bengal, Eastern India. XRD study confirmed the presence of metallic iron. A higher BET surface area (143.163 m$^2$/g) indicated that nZVI might act as a potential adsorbent for phosphate and could efficiently adsorb phosphate from wastewater. Various parameters, e.g., initial phosphate concentration, adsorbent dosage, pH, and ionic strength, were optimized. A maximum $PO_4^{3-}$ removal rate of ~96% was achieved at pH 2. Ionic strength did not affect the removal of $PO_4^{3-}$ in the presence of 0.01 moles of NaCl. The coexisting anions chloride and sulphate did not affect the phosphate removal process. However, carbonate anions strongly affected phosphate removal. Equilibrium and kinetic studies depicted that the adsorption process was a good fit with the Temkin isotherm model and the pseudo-2nd-order kinetic model, respectively. Some thermodynamic parameters, e.g., $\Delta G^0$, $\Delta S^0$, and $\Delta H^0$, were estimated, which suggested that the adsorption of phosphate on the nZVI surface is endothermic in nature and spontaneous. The reusability test of nZVI proved that it could be reused up to the fifth cycle and be

applied in large-scale industries. Also, the phosphate RE from Saheb Bandh water was about 86.5% up to a reaction time of 120 min, and a lower pH value (pH 2) facilitated achieving maximum RE. Furthermore, the real water (Saheb Bandh water) sample results demonstrate that the synthesized and cost-effective nZVI is a promising nanomaterial for the removal of $PO_4^{3-}$ from contaminated wastewater. From all these perspectives, the nZVI system can be prepared as a bed for industrial application. Then real water samples can be passed through this bed to obtain clean and hygienic water. Moreover, the amount of clean water produced can be determined. Also, how many times the same nZVI bed can be used to make phosphate-free water can be evaluated. Ultimately, in this study, it was proved that nZVI was a suitable adsorbent for effective removal of $PO_4^{3-}$, a dangerous pollutant found in aqueous bodies. A cost estimation analysis was done for lab-scale preparation of nZVI. Table S4 (Supplementary file) reveals that only 125.478 INR has been spent on the synthesis of 1 g nZVI. Thus, only 70.267 INR is needed for the complete removal of $PO_4^{3-}$-containing wastewater of 1 L volume.

Although, in our work, synthesized nZVI has been proved to be a feasible nanomaterial for efficient removal of $PO_4^{3-}$ from wastewater, some problems associated with this application should be fixed.

Rapid corrosion is one of the most serious problems that limit its application. nZVI produces Fe(II), Fe(III), and hydrogen while in contact with polluted water. These generated nZVI corrosion by-products block the active site on the nZVI surface, which leads to surface passivation. As a result, the removal rate of contaminants is reduced. In this context, research focus should be on the development of polymer, carbon-supported nZVI-based nanomaterial to prevent its corrosion during reaction. In addition, the selectivity of nZVI for removing specific contaminants and multicomponents in the complex system is poor, which should be improved. Moreover, it is essential to prove the practicability of nZVI in large-scale applications, and its effectiveness, safety, and economy should also be guaranteed. Today, knowledge about the probable hazards caused by the utilization of nZVI is inadequate. The toxicity of nZVI materials must be taken into account before applying them for environmental purification. Hence, efforts should be taken to elucidate the toxicity mechanism of nZVI and evaluate its environmental hazards for prescribing a suitable standard.

## CONSENT TO PUBLISH

The authors confirm that the final version of the manuscript has been reviewed, approved, and consented for publication by all authors.

## AUTHORS' CONTRIBUTIONS

Material preparation (zerovalent iron preparation), laboratory work, manuscript draft writing, data analysis, data interpretation, editing, and formatting of the manuscript were done by I.S. Laboratory work and data collection were performed by S.S. Planning and design of work, analysis, interpretation of data, and revision of the manuscript were done by M.R. Real water sample collection and the design of the project were done by S.G. Oversight and leadership responsibility for the project planning and execution including mentorship to the core team and funding acquisition were taken up by R.S. Finally, all authors read and approved the final manuscript.

## DATA AVAILABILITY STATEMENT

All relevant data are included in the paper or its Supplementary Information.

## CONFLICT OF INTEREST

The authors state that there is no conflict to declare.

## REFERENCES

Adam, C. 2011 *Case Study – 'Phosphorus Recovery from Sewage Sludge-Results of the European FP6-and FP7-Projects SUSAN and SUSYPHOS'*.

Ai, Z., Cheng, Y., Zhang, L. & Qiu, J. 2008 Efficient removal of Cr (VI) from aqueous solution with Fe@Fe$_2$O$_3$ core– shell nanowires. *Environmental Science & Technology* **42** (18), 6955–6960.

Aiken, G. R., Hsu-Kim, H. & Ryan, J. N. 2011 Influence of Dissolved Organic Matter on the Environmental Fate of Metals, Nanoparticles, and Colloids. *Environmental Science & Technology* **45** (8), 3196–3201.

An, J. S., Back, Y. J., Kim, K. C., Cha, R., Jeong, T. Y. & Chung, H. K. 2014 Optimization for the removal of orthophosphate from aqueous solution by chemical precipitation using ferrous chloride. *Environmental Technology* **35**, 1668–1675.

Ansari, A. A., Gill, S. S. & Khan, F. A. 2011 Eutrophication: causes, consequences and control, Vol.104. In: *Eutrophication: Threat to Aquatic Ecosystems (Chapter 7)*, pp. 143–170. doi:10.1007/978-90-481-9625-8_7.

Arshadi, M., Gholtash, J. E., Zandi, H. & Foroughifard, S. 2015a Phosphate removal by a nano-biosorbent from the synthetic and real (Persian Gulf) water samples. *RSC Advances* **5** (54), 43290–43302.

Arshadi, M., Zandi, H., Akbari, J. & Shameli, A. 2015b Ferrocene functionalized nanoscale mixed-oxides as a potent phosphate adsorbent from the synthetic and real (Persian Gulf) waters. *Journal of Colloid and Interface Science* **450**, 424–433.

Banerjee, S., Mukherjee, S., LaminKa-Ot, A., Joshi, S. R., Mandal, T. & Halder, G. 2016 Biosorptive uptake of Fe$^{2+}$, Cu$^{2+}$ and As$^{5+}$ by activated biochar derived from *Colocasia esculenta*: isotherm, kinetics, thermodynamics, and cost estimation. *Journal of Advanced Research* **7** (5), 597–610.

Brandl, F., Bertrand, N., Lima, E. M. & Langer, R. 2015 Nanoparticles with photoinduced precipitation for the extraction of pollutants from water and soil. *Nature Communications* **6** (1), 1–10.

Chen, S., Zhang, J., Zhang, C., Yue, Q., Li, Y. & Li, C. 2010 Equilibrium and kinetic studies of methyl orange and methyl violet adsorption on activated carbon derived from *Phragmites australis*. *Desalination* **252** (1–3), 149–156.

Chouyyok, W., Wiacek, R. J., Pattamakomsan, K., Sangvanich, T., Grudzien, R. M., Fryxell, G. E. & Yantasee, W. 2010 Phosphate removal by anion binding on functionalized nanoporous sorbents. *Environmental Science & Technology* **44** (8), 3073–3078.

Cleary, J., Slater, C. & Diamond, D. 2009 Analysis of phosphate in wastewater using an autonomous microfluidics-based analyser. *World Academy of Science, Engineering and Technology* **28**, 196–199.

Cordell, D., Drangert, J.-O. & White, S. 2009 The story of phosphorus: global food security and food for thought. *Global Environmental Change* **19** (2), 292–305.

de-Bashan, L. E. & Bashan, Y. 2004 Recent advances in removing phosphorus from wastewater and its future use as fertilizer (1997–2003). *Water Research* **38** (19), 4222–4246.

Dolatabadi, M. & Ahmadzadeh, S. 2019 A rapid and efficient removal approach for degradation of metformin in pharmaceutical wastewater using electro-Fenton process; optimization by response surface methodology. *Water Science and Technology* **80** (4), 685–694.

Domingos, R. F., Tufenkji, N. & Wilkinson, K. J. 2009 Aggregation of titanium dioxide nanoparticles: role of a fulvic acid. *Environmental Science & Technology* **43** (5), 1282–1286.

Dutta, G., Gupta, S. & Gupta, A. 2019 Lake hydro geochemistry: an implication to chemical weathering, ion-exchange phenomena and metal interaction. *Pollution* **5** (4), 803–819.

Florida State Legislature 1994 *The Florida Legislature Passed the Everglades Forever Act, Which Directed the State of Florida to Develop a Phosphorus Criterion for the Everglades Protection Area*.

Fu, H. & Quan, X. 2006 Complexes of fulvic acid on the surface of hematite, goethite, and akaganeite: FTIR observation. *Chemosphere* **63** (3), 403–410.

Fu, F., Dionysiou, D. D. & Liu, H. 2014 The use of zero-valent iron for groundwater remediation and wastewater treatment: a review. *Journal of Hazardous Materials* **267**, 194–205.

Fytianos, K., Voudrias, E. & Raikos, N. 1998 Modelling of phosphorus removal from aqueous and wastewater samples using ferric iron. *Environmental Pollution* **101**, 123–130.

Gao, Q., Wang, C. Z., Liu, S., Hanigan, D., Liu, S. T. & Zhao, H. Z. 2019 Ultrafiltration membrane microreactor (MMR) for simultaneous removal of nitrate and phosphate from water. *Chemical Engineering Journal* **355**, 238–246.

Garg, V. K., Kumar, R. & Gupta, R. 2004 Removal of malachite green dye from aqueous solution by adsorption using agro-industry waste: a case study of Prosopis cineraria. *Dyes and Pigments* **62** (1), 1–10.

Ge, X., Song, X., Ma, Y., Zhou, H., Wang, G., Zhang, H., Zhang, Y., Zhao, H. & Wong, P. K. 2016 Fabrication of hierarchical iron-containing MnO$_2$ hollow microspheres assembled by thickness-tunable nanosheets for efficient phosphate removal. *Journal of Materials Chemistry A* **4** (38), 14814–14826.

Ghoreishi, S. M. & Haghighi, R. 2003 Chemical catalytic reaction and biological oxidation for treatment of non-biodegradable textile effluent. *Chemical Engineering Journal* **95** (1–3), 163–169.

Ghosh, A., Dutta, S., Mukherjee, I., Biswas, S., Chatterjee, S. & Saha, R. 2017 Template-free synthesis of flower-shaped zero-valent iron nanoparticle: role of hydroxyl group in controlling morphology and nitrate reduction. *Advanced Powder Technology* **28** (9), 2256–2264.

Ghosh, A., Meshram, N. K. & Saha, R. 2019 Glycerol-mediated synthesis of nanoscale zerovalent iron and its application for the simultaneous reduction of nitrate and alachlor. *Environmental Science and Pollution Research* **26** (12), 11951–11961.

Gouider, M., Mlaik, N., Feki, M. & Sayadi, S. 2011 Integrated physicochemical and biological treatment process for fluoride and phosphorus removal from fertilizer plant wastewater. *Water Environment Research* **83** (8), 731–738.

Ihsanullah Asmaly, H. A., Saleh, T. A., Laoui, T., Kumar Gupta, V. & Atieh, M. A. 2015 Enhanced adsorption of phenols from liquids by aluminumoxide/carbon nanotubes: comprehensive study from synthesis to surface properties. *Journal of Molecular Liquids* **206**, 176–182.

Jansson, T., Andersen, H. E., Gustafsson, B. G., Hasler, B., Höglind, L. & Choi, H. 2019 Baltic Sea eutrophication status is not improved by the first pillar of the European Union Common Agricultural Policy. *Regional Environmental Change* **19**, 2465–2476.

Johnson, R. L., Johnson, G. O., Nurmi, J. T. & Tratnyek, P. G. 2009 Natural organic matter enhanced mobility of nano zerovalent iron. *Environmental Science & Technology* **43** (14), 5455–5460.

Jupp, A. R., Beijer, S., Narain, G. C., Schipper, W. & Slootweg, J. C. 2021 Phosphorus recovery and recycling – closing the loop. *Chemical Society Reviews* **50**, 87–101.

Kamaraj, R., Pandiarajan, A., Jayakiruba, S., Naushad, M. & Vasudevan, S. 2016 Kinetics, thermodynamics and isotherm modeling for removal of nitrate from liquids by facile one-pot electrosynthesized nano zinc hydroxide. *Journal of Molecular Liquids* **215**, 204–211.

Kanel, S. R., Manning, B., Charlet, L. & Choi, H. 2005 Removal of arsenic(III) from groundwater by nanoscale zero-valent iron. *Environmental Science & Technology* **39** (5), 1291–1298.

Kumar, R. & Pal, P. 2015 Assessing the feasibility of N and P recovery by struvite precipitation from nutrient-rich wastewater: a review. *Environmental Science and Pollution Research* **22** (22), 17453–17464.

Langford, J. I. & Wilson, A. J. C. 1978 Scherrer after sixty years: a survey and some new results in the determination of crystallite size. *Journal of Applied Crystallography* **11** (2), 102–113.

Li, C., Ma, J., Shen, J. & Wang, P. 2009 Removal of phosphate from secondary effluent with $Fe^{2+}$ enhanced by $H_2O_2$ at nature pH/neutral pH. *Journal of Hazardous Materials* **166**, 891–896.

Li, L., Zhu, Q., Man, K. & Xing, Z. 2017 Fluoride removal from liquid phase by Fe–Al–La trimetal hydroxides adsorbent prepared by iron and aluminum leaching from red mud. *Journal of Molecular Liquids* **237**, 164–172.

Liu, Y., Phenrat, T. & Lowry, G. V. 2007 Effect of TCE concentration and dissolved groundwater solutes on NZVI-promoted TCE dechlorination and H2 evolution. *Environmental Science & Technology* **41** (22), 7881–7887.

Meena, A. K., Mishra, G. K., Rai, P. K., Rajagopal, C. & Nagar, P. N. 2005 Removal of heavy metal ions from aqueous solutions using carbon aerogel as an adsorbent. *Journal of Hazardous Materials* **122** (1–2), 161–170.

Mehta, C. M., Khunjar, W. O., Nguyen, V., Tait, S. & Batstone, D. J. 2015 Technologies to recover nutrients from waste streams: a critical review. *Critical Reviews in Environmental Science and Technology* **45** (4), 385–427.

Mishra, S. P., Das, M. & Dash, U. N. 2010 Review on Adverse Effects of Water Contaminants Like Arsenic, Fluoride and Phosphate and their Remediation. *Journal of Scientific and Industrial Research* **69**, 249–253.

Morillo, D., Uheida, A., Pérez, G., Muhammed, M. & Valiente, M. 2015 Arsenate removal with 3-mercaptopropanoic acid-coated superparamagnetic iron oxide nanoparticles. *Journal of Colloid and Interface Science* **438**, 227–234.

Najafi, F., Moradi, O., Rajabi, M., Asif, M., Tyagi, I., Agarwal, S. & Gupta, V. K. 2015 Thermodynamics of the adsorption of nickel ions from aqueous phase using graphene oxide and glycine functionalized graphene oxide. *Journal of Molecular Liquids* **208**, 106–113.

Nancharaiah, Y., Mohan, S. V. & Lens, P. 2016 Recent advances in nutrient removal and recovery in biological and bioelectrochemical systems. *Bioresource Technology* **215**, 173–185.

Novillo, C., Guaya, D., Avendaño, A. A. P., Armijos, C., Cortina, J. L. & Cota, I. 2014 Evaluation of phosphate removal capacity of Mg/Al layered double hydroxides from aqueous solutions. *Fuel* **138**, 72–79.

Piccin, J. S., Dotto, G. L. & Pinto, L. A. A. 2011 Adsorption isotherms and thermochemical data of FD&C Red n 40 binding by chitosan. *Brazilian Journal of Chemical Engineering* **28** (2), 295–304.

Priddy, S. A. & Hanley, T. R. 2003 Effect of agitation on removal of acetic acid from pretreated hydrolysate by activated carbon. *Applied Biochemistry and Biotechnology* **105–108**, 353–364.

Quesada, H. B., de Araujo, T. P., Vareschini, D. T., de Barros, M. A. S. D., Gomes, R. G. & Bergamasco, R. 2020 Chitosan, alginate and other macromolecules as activated carbon immobilizing agents: a review on composite adsorbents for the removal of water contaminants. *International Journal of Biological Macromolecules* **164**, 2535–2549.

Riahi, F., Bagherzadeh, M. & Hadizadeh, Z. 2015 Modification of $Fe_3O_4$ superparamagnetic nanoparticles with zirconium oxide; preparation, characterization and its application toward fluoride removal. *RSC Advances* **5** (88), 72058–72068.

Rotzetter, A. C. C., Kellenberger, C. R., Schumacher, C. M., Mora, C., Grass, R. N., Loepfe, M. & Stark, W. J. 2013 Combining phosphate and bacteria removal on chemically active filter membranes allows prolonged storage of drinking water. *Advanced Materials* **25** (42), 6057–6063.

Roy, E. D. 2017 Phosphorus recovery and recycling with ecological engineering: a review. *Ecological Engineering* **98**, 213–227.

Ryu, A., Jeong, S. W., Jang, A. & Choi, H. 2011 Reduction of highly concentrated nitrate using nanoscale zero-valent iron: effects of aggregation and catalyst on reactivity. *Applied Catalysis B: Environmental* **105** (1–2), 128–135.

Shiau, C. Y. & Pan, C. C. 2004 Adsorption of basic dyes from aqueous solution by various adsorbents. *Separation Science and Technology* **39**, 1733–1750.

Siddiqi, S. Z. & Chandrasekhar, S. V. A. 2010 Hydrobiology of raw water reservoir at Adra, Purulia District, West Bengal. *Records of the Zoological Survey of India* **110** (1), 83–91.

Simonin, J. P. 2016 On the comparison of pseudo-first order and pseudo-second order rate laws in the modeling of adsorption kinetics. *Chemical Engineering Journal* **300**, 254–263.

Sirianuntapiboon, S., Chairattanawan, K. & Jungphungsukpanich, S. 2006 Some properties of a sequencing batch reactor system for removal of vat dyes. *Bioresource Technology* **97** (10), 1243–1252.

Stensel, H. D. 1991 *Principles of Biological Phosphorus Removal: Phosphorus and Nitrogen Removal From Municipal Wastewaters Principles and Practice*, 2nd edn. H. K. Lewis, London.

Sun, Y. P., Li, X. Q., Zhang, W. X. & Wang, H. P. 2007 A method for the preparation of stable dispersion of zero-valent iron nanoparticles. *Colloids and Surfaces A: Physicochemical and Engineering Aspects* **308** (1–3), 60–66.

Sun, H., Zhou, Q., Zhao, L. & Wu, W. 2021 Enhanced simultaneous removal of nitrate and phosphate using novel solid carbon source/zero-valent iron composite. *Journal of Cleaner Production* **289**, 125757.

Tao, W., Fattah, K. P. & Huchzermeier, M. P. 2016 Struvite recovery from anaerobically digested dairy manure: a review of application potential and hindrances. *Journal of Environmental Management* **169**, 46–57.

Tran, D. N., Kabiri, S., Wang, L. & Losic, D. 2015 Engineered graphene–nanoparticle aerogel composites for efficient removal of phosphate from water. *Journal of Materials Chemistry A* **3** (13), 6844–6852.

UNEP 2011 *Emerging Issues in Our Global Environment. UNEP Year Book – 2011*. United Nations Environment Programme, Nairobi. Available from: http://www.unep.org/yearbook/2011.

U.S. Environmental Protection Agency (USEPA) 1986 *Quality Criteria for Water 1986*. Office of Water, Regulation and Standard, Washington, DC, p. 20460, EPA 440/5-86-001.

Vijayakumar, G., Yoo, C. K., Elango, K. G. P. & Dharmendirakumar, M. 2010 Adsorption characteristics of rhodamine B from aqueous solution onto baryte. *Clean – Soil, Air, Water* **38** (2), 202–209.

Wang, C. B. & Zhang, W. X. 1997 Synthesizing nanoscale iron particles for rapid and complete dechlorination of TCE and PCBs. *Environmental Science & Technology* **31** (7), 2154–2156.

Wang, L. K., Hung, Y. T. & Shammas, N. K. 2005 *Physicochemical Treatment Processes*, Vol. 3. Humana Press, Totowa, NJ.

Wang, H., Wang, N., Wang, B., Zhao, Q., Fang, H., Fu, C. & Jiang, Q. 2016 Antibiotics in drinking water in Shanghai and their contribution to antibiotic exposure of school children. *Environmental Science & Technology* **50** (5), 2692–2699.

Wen, Z., Zhang, Y. & Dai, C. 2014 Removal of phosphate from aqueous solution using nanoscale zerovalent iron (nZVI). *Colloids and Surfaces A: Physicochemical and Engineering Aspects* **457**, 433–440.

Wu, D., Shen, Y., Ding, A., Mahmood, Q., Liu, S. & Tu, Q. 2013a Effects of nanoscale zero-valent iron particles on biological nitrogen and phosphorus removal and microorganisms in activated sludge. *Journal of Hazardous Materials* **262**, 649–655.

Wu, D., Shen, Y., Ding, A., Qiu, M., Yang, Q. & Zheng, S. 2013b Phosphate removal from aqueous solutions by nanoscale zero-valent iron. *Environmental Technology* **34** (18), 2663–2669.

Yuan, L., Qiu, Z., Yang, J., Li, Z., Farooq, U., Lu, Y. & Lyu, S. 2018 Adsorption performance and mechanism for phosphate removal by cerium hydroxide loaded on molecular sieve. *Journal of the Taiwan Institute of Chemical Engineers* **93**, 450–460.

Zhang, Q., Liu, H., Chen, T., Chen, D., Li, M. & Chen, C. 2017 The synthesis of NZVI and its application to the removal of phosphate from aqueous solutions. *Water, Air, & Soil Pollution* **228** (9), 1–10.

Zhao, Y., Wang, J., Luan, Z., Peng, X., Liang, Z. & Shi, L. 2009 Removal of phosphate from aqueous solution by red mud using a factorial design. *Journal of Hazardous Materials* **165** (1–3), 1193–1199.

Zhou, J., Yang, S., Yu, J. & Shu, Z. 2011 Novel hollow microspheres of hierarchical zinc–aluminum layered double hydroxides and their enhanced adsorption capacity for phosphate in water. *Journal of Hazardous Materials* **192** (3), 1114–1121.